THE JOURNAL OF
PHYSICAL
CHEMISTRY A

VOLUME 106, NUMBER 25, JUNE 27, 2002

FEATURE ARTICLE

State-Selected and State-to-State Ion−Molecule Reaction Dynamics

Cheuk-Yiu Ng*

Department of Chemistry, University of California at Davis, One Shields Ave., Davis, California 95616

Received: January 10, 2002; In Final Form: April 8, 2002

A unique triple-quadrupole double-octopole (TQDO) photoionization mass spectrometer has been developed for total cross section measurements of state-selected ion−molecule reactions. By employing this TQDO apparatus, we have recently examined the absolute total cross sections for a series of state-selected ion−molecule reactions involving $Ar^+(^2P_{3/2,1/2})$, $O^+(^4S, ^2D, ^2P)$, and organosulfur ions (CH_3SH^+, $CH_3CH_2SH^+$, and $CH_3SCH_3^+$) in their ground states. The cross section measurements, together with product ion kinetic energy analyses, have provided convincing evidence that the $Ar^+(^2P_{3/2,1/2}) + CO_2$ (CO, N_2, O_2) reactions proceed via a charge-transfer predissociation mechanism. The comparison of absolute cross sections for product ions formed in the dissociative charge transfer of $Ar^+(^2P_{3/2,1/2}) + CO_2$ (CO, N_2, O_2) and those produced in photoionization of CO_2 (CO, N_2, O_2) suggests that product ions formed by dissociative charge transfer are also produced by photoionization via a similar set of excited predissociative states of CO_2^+ (CO^+, N_2^+, O_2^+). By preparing CH_3SH^+, $CH_3CH_2SH^+$, and $CH_3SCH_3^+$ in their ground states by photoionization of the corresponding neutrals, we have examined the dissociation of these ions via collision activation. Equipped with two radio frequency octopole ion guide reaction gas cells, the TQDO apparatus has allowed the identification of the isomeric structure of product ions by using the charge-transfer probing method. Strong preference is observed for C−S and C−C bond scissions, leading to the formation of CH_3^+ from CH_3SH^+, $CH_3CH_2^+$, and CH_2SH^+ from $CH_3CH_2SH^+$, and CH_3S^+ from $CH_3SCH_3^+$ as compared to C−H and S−H bond breakages. The observation of these bond selective dissociation reactions is contrary to that found in photoionization of CH_3SH, CH_3CH_2SH, and CH_3SCH_3 and is indicative of nonstatistical behavior for collision-induced dissociation of these organosulfur ions. An application of the radio frequency ion-guide for state-selection of $O^+(^4S, ^2D, ^2P)$ prepared by the dissociative charge-transfer reactions of He^+ (Ne^+, Ar^+) + O_2 is described. The success of this method has made possible the absolute total cross section measurement of the state-selected ion−molecule reactions $O^+(^4S, ^2D, ^2P) + N_2$ (O_2, H_2, D_2, CO_2, H_2O), which are considered as the most important set of reactions in the Earth's ionosphere.

1. Introduction

State-selected and state-to-state studies of unimolecular and bimolecular processes are the cornerstone for fundamental understanding of molecular reaction dynamics.[1,2] The fact that absolute cross sections can be obtained directly by first principle calculations makes accurate experimental cross sections important in providing stringent tests not only for the theoretical dynamical model, but also for the ab initio interaction potentials used in the calculations. However, the experimental challenges for reactant state-selection and product state-identification are high. Thus, the advancement of state-selected and state-to-state

---

* To whom correspondence should be addressed. E-mail address: cyng@chem.ucdavis.edu.

10.1021/jp020055i CCC: $22.00

chemistry depends critically on the development of general experimental schemes for reactant state preparation and product state detection.

As an experimental method to provide accurate absolute cross section data for first-principle theoretical developments in molecular dynamics, ion−molecule reaction studies offer many attractive features.[2] Owing to the ease in varying the collision energy and the efficient collection of ions, absolute total cross section (σ) measurements for ion−molecule reactions can be made with good precision over a significantly broader range of center-of-mass collision energies ($E_{c.m.}$) than can be achieved in neutral−neutral scattering studies. The radio frequency (RF) octopole ion-guide technique[3] has been well established as a general method for absolute cross section measurements for ion−molecule reactions covering the $E_{c.m.}$ range of chemical interest from thermal energies to well above 10 eV.

It has also been demonstrated that photoionization is the most versatile method for the preparation of state- or energy-selected reactant ions.[4−6] Among photoionization schemes, single photon ionization, which usually occurs in the vacuum ultraviolet (VUV), is the most general and cleanest photoionization method.[5,6] Because of the fine control in photon energy, ions in their ground states can be easily prepared with 100% purity by photoionization at the IE of the neutral precursor molecules.[6] For specific cases, ions with a known distribution of internal states can also be produced by the simple photoionization method.[6] The more advanced VUV threshold photoelectron (TPE)-secondary photoion coincidence (TPESICO) method[5] has also been used successfully for state-selected ion−molecule reactions studies.

Although reactant and products ions involved can be unambiguously identified by mass spectrometer, the identification of product ion structures remains a great challenge in ion−molecule reaction studies. Polyatomic ions produced in an ion−molecule reaction may exist in various isomeric forms. Thus, the ability to determine of the isomeric structure or distribution of structures of polyatomic ions is fundamental for a detailed experiment study. A common method in mass spectrometry to probe the chemical structure of a polyatomic ion is to examine the fragmentation pattern via collision activation.[7] Considering the fact that polyatomic molecules with different isomeric structures have distinctly different ionization energies (IEs), we expected that isomeric structures of polyatomic ions can be probed by using appropriate charge-transfer reactions.[8] Furthermore, since the reactivity of an ion usually depends on its internal energy, the internal states or energies for product ions can also be probed using appropriate ion−molecule reactions.[6]

Taking into account the above considerations, we have developed a triple-quadrupole double-octopole (TQDO) photoionization mass spectrometer for state-selected and state-to-state ion−molecule reaction studies.[6,8−26] In this article, an overview on recent representative experiments concerning cross section measurements of the dissociative charge transfer (DCT) reactions[9,10,12,13,16] of $Ar^+(^2P_{3/2,1/2}) + CO_2$ (N_2, CO, O_2) and the collision induced dissociation (CID) reactions[23−26] of CH_3SH^+ ($CH_3CH_2SH^+$, $CH_3SCH_3^+$) + Ar is described. The cross sections of these reactions have been compared to those observed in photoionization.[16] On the basis of product ion kinetic energy analyses, we have proposed a charge-transfer predissociative mechanism for $Ar^+(^2P_{3/2,1/2}) + CO_2$ (N_2, CO, O_2). We have obtained strong evidence that the CID reactions of CH_3SH^+, $CH_3CH_2SH^+$, and $CH_3SCH_3^+$ are nonstatistical, favoring product ions formed by scission of the C−S and C−C bonds. A consistent mechanism has emerged based on the cross section measurements and the structural determination of product ions formed in the CID reactions involving CH_3SH^+, $CH_3CH_2SH^+$, and $CH_3SCH_3^+$, providing a rationalization for the selective bond scission processes observed in these reactions.

Other than the motivation for fundamental understanding of molecular reaction dynamics, the main driving force for absolute state-selected cross section measurements of ion−neutral processes is the need for modeling of plasma environments, such as in planetary atmospheres[27,28] and aerospace[29−33] environments, where hypersonic nonequilibrium flow conditions prevail. A major part of our recent efforts has been devoted to ion chemistry studies relevant to planetary atmospheres.[11,14−22] Ions appearing in planetary atmospheres are mostly formed by electron impact and solar ultraviolet and VUV dissociation and ionization processes.[27,28] Through chemical interactions, ions initially formed by these processes influence the concentrations and temperatures of electrons, ions, and neutral molecules in the atmospheres. Quantitative in situ and laboratory measurements of rate constants and cross sections for reactions involving relevant ionic species are of importance for realistic modeling of reaction cycles in planetary atmospheres.[34−36]

The O^+ ions formed with a branching ratio[37−40] 0.43:0.29:0.28 for $O^+(^4S)$:$O^+(^2D)$:$O^+(^2P)$ by solar VUV photoionization of O atoms are the most abundant ions in the F-region of the Earth's atmosphere.[37,41] Because the excited $O^+(^2D)$ and $O^+(^2P)$ ions, which lie 3.324 and 5.017 eV above the $O^+(^4S)$ ground state, are metastable with radiative lifetimes of 3.6 h and 4.57 s, respectively, knowledge about the decay and reaction pathways for $O^+(^2D)$ and $O^+(^2P)$ are essential for our understanding of the ion chemistry in the ionosphere.[34−36,41] It is known that the rates for radiative recombination of O^+ with electrons are several orders of magnitude smaller than those for dissociative recombination of N_2^+, O_2^+ and NO^+ with electrons.[42,43] Thus, the major decay pathways for $O^+(^4S, ^2D, ^2P)$ and electrons first involve the reactions between $O^+(^4S, ^2D, ^2P)$ and atmospheric gases. Product O_2^+ ions formed in the charge-transfer reaction of $O^+ + O_2$ are known to undergo rapid dissociative recombination reactions with electrons, giving rise to excited oxygen atoms.[44] The emission of $O(^1S)$ atoms thus formed is the source of the 5577 Å green aurora, which is a prominent spectral feature in the night sky and is extensively used by aeronomers for probing the chemistry and dynamics of the ionosphere.[45] Ion−molecule processes involving $O^+(^4S, ^2D, ^2P)$ also play an important role in the ionosphere chemistry of other planets such as Mars and Venus.[28] The ion−molecule reaction $O^+(^4S, ^2D, ^2P) + H_2$ is relevant to the study of H_2-rich interstellar cloud, where OH^+ ions initially formed further react with H_2 to yield H_2O^+ and H_3O^+ molecular ions.[46−48] Although most reactions involving $O^+(^4S)$ have been studied extensively by a variety of techniques,[11,15,17] the reactions involving $O^+(^2D)$ and $O^+(^2P)$ have not been examined directly. Using the TQDO mass spectrometer, we have designed an efficient method for preparing state-selected $O^+(^2D)$ and $O^+(^2P)$ with high purity for absolute total cross section measurements.[18] As expected, the cross sections for most reactions involving $O^+(^2D)$ and $O^+(^2P)$ are significantly greater than those of $O^+(^4S)$.[11,15,17−22]

In addition to the overview of previous experiments, recent efforts[49−51] of applying the high resolution pulsed field ionization (PFI) schemes for preparation of state-selected reactant is described. We have recently demonstrated a high-resolution synchrotron based PFI-photoelectron (PFI−PE)-photoion coincidence (PFI−PEPICO) technique,[50−58] achieving a resolution of ≤ 1 meV (full-width-at-half-maximum, fwhm) for ion internal energy selection. The PFI−PEPICO technique has been suc-

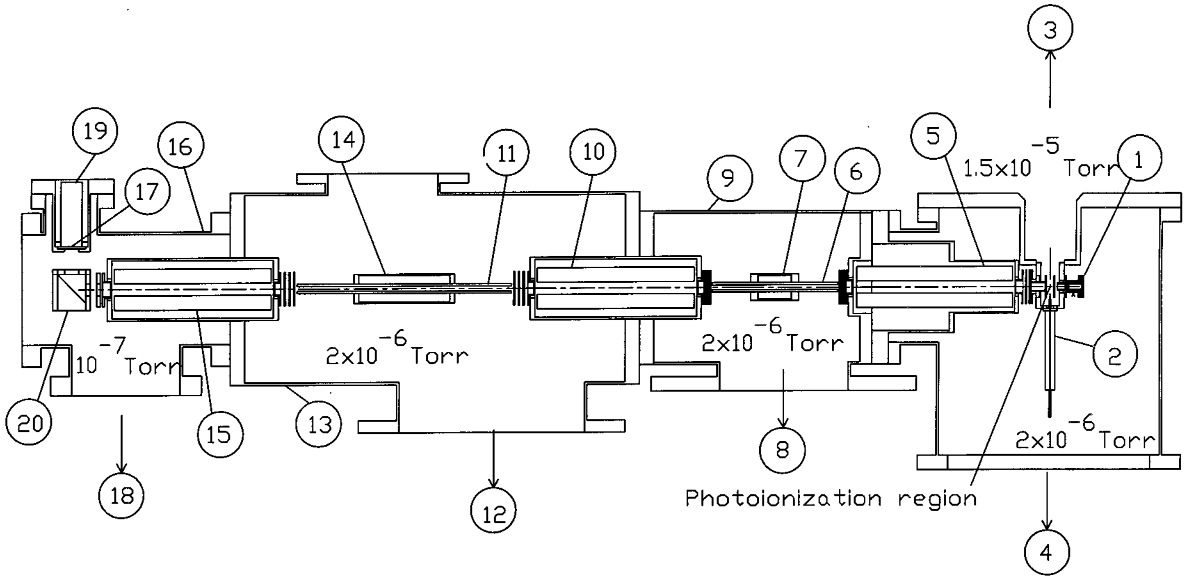

Figure 1. Schematic of the TQDO photoionization mass spectrometer for absolute total cross section measurements. (1) electron impact ionization ion source, (2) atomic or molecular nozzle beam, (3) to Freon-trapped 6" diffusion pump, (4) to turbomolecular pump (500 L/s), (5) reactant QMS, (6) lower RF octopole ion guide, (7) lower RFOIGGC, (8) to turbomolecular pump (500 L/s), (9) the lower RF octopole ion guide chamber, (10) middle QMS, (11) upper RF octopole ion guide, (12) to turbomolecular pump (500 L/s), (13) upper RF octopole ion guide chamber, (14) upper RFOIGGC, (15) product QMS, (16) detector chamber, (17) plastic scintillator window, (18) to turbomolecular pump (250 L/s) (19) photomultiplier tube, (20) aluminum ion target.[6,18]

cessfully applied to state- or energy-selected unimolecular dissociation studies of a range of simple ions.[52−58] Progress has also been made in the development of the PFI−PE-secondary ion coincidence (PFI−PESICO) scheme for state-selected ion−molecule reaction studies. We are hopeful that the PFI−PESICO scheme would become a general scheme for state- or energy-selected ion−molecule reaction dynamics studies with achievable resolutions similar to those demonstrated in PFI−PE measurements.

2. Triple-Quadrupole Double-Octopole Photoionization Mass Spectrometer

The experimental arrangement and procedures of using the TQDO photoionization mass spectrometer for absolute total cross section measurements have been described in detail.[6,18] As shown in Figure 1, the TQDO apparatus consists of, in sequential order, a VUV photoionization ion source, a reactant quadrupole mass spectrometer (QMS) (5), a lower RF octopole ion guide reaction gas cell (RFOIGGC) [(6)+(7)], a middle QMS (10), an upper RFOIGGC [(11) +(14)], a product QMS (15), and a Daly type scintillation ion detector [(17)+(19)+-(20)]. When a VUV photoionization ion source is used, the neutral precursor molecules are introduced into the photoionization region in the form of a free jet. Tunable VUV radiation in the range from ∼7.5−21.4 eV (580−1650 Å) with a wavelength resolution of 3−6 Å (fwhm) is produced by discharge lamps, together with a differentially pumped windowless 0.2-m monochromator (McPherson 234) system. The intensity for dispersed VUV radiation is monitored by a tungsten photoelectric detector. An electron impact ionization ion source (1) has also been installed, such that it can be used in place of the photoionization ion source depending on the requirement of the experiment. The TQDO apparatus is partitioned into five chambers, which are separately evacuated by turbomolecular pumps.

The application of an RF only octopole field as an ion guide for absolute cross section measurements was pioneered by Teloy and Gerlich.[3] An electric multipole structure with $2n$ poles is formed by $2n$ rods symmetrically spaced on an inscribed circle with a diameter of $2r_o$. The principle of the RF electric multipole field for trapping and guiding ions (charge $= q$, mass $= m$) is based on the fact that with a sufficiently high RF amplitude (V_o) and an appropriate frequency (ω), a sufficiently high effective potential [$V_{\mathrm{eff}}(r)$] is established to confine the ions.[3] Under the limit of certain operating conditions, the expression for $V_{\mathrm{eff}}(r)$ of an octopole ($n = 4$) is

$$V_{\mathrm{eff}}(r) = 4\,[(q^2\,V_o^{\,2})/(m\,\omega^2\,r_o2)]\,(r/r_o)^6 \qquad (1)$$

This potential is close to a square well, providing a tubular trapping volume with a low potential near the center and a rapidly increasing potential wall near the poles of the octopole.

3. Highlights of Recent Work

3.1. Dissociative Charge Transfer of $\mathbf{Ar^+(^2P_{3/2,1/2}) + CO_2}$ $\mathbf{(CO, N_2, O_2)}$. In these studies,[9,10,12,13,16] the Ar^+ reactant ions in pure $^2P_{3/2}$ state or in a 2:1 mixture of $^2P_{3/2}$ and $^2P_{1/2}$ states are prepared by photoionization of Ar at photon energies below and above the IE for $Ar^+(^2P_{1/2})$, respectively. The reactant Ar^+ ions formed in the photoionization region are extracted and mass selected by the reactant QMS before reacting with neutral reactant gases in the upper RFOIGGC. The middle QMS and the lower RF octopole are operated in the RF-only mode to pass all ions. The reactant $Ar^+(^2P_{3/2,1/2})$ and product ions formed in the upper RFOIGGC are mass selected by the product QMS and detected by the ion detector. The laboratory kinetic energy (E_{lab}) for reactant Ar^+ is measured by the retarding potential energy method using the upper octopole ion guide. The kinetic energy distributions for product ions are measured by their retarding potential energy curves obtained using the ion lenses situated at the exit of the upper octopole ion guide.

The absolute total cross section measurements of product ions formed in the $Ar^+(^2P_{3/2,1/2})$ + CO (N_2, O_2) reactions, together with product ion kinetic energy analyses, support a charge-transfer predissociation mechanism.[9,10,12,13,16] With the exception for the formation of charge-transfer N_2^+, CO^+, and O_2^+, all other dissociative and reactive channels leading to the formation of C^+, O^+, N^+, ArN^+, ArO^+, and ArC^+ from these reactions are highly endothermic. Thus, the cross sections for these latter ions are expected to be insignificant. Surprisingly, the σ values for the dissociative and reactive channels of the $Ar^+(^2P_{3/2,1/2})$ + CO (N_2, O_2) reactions are found to be high. The appearance energies (AEs) observed for N^+ (C^+, O^+) formed in these reactions are in agreement with their thermochemical thresholds. The kinetic energy analyses indicate that product ArC^+, ArN^+, and ArO^+ ions are scattered in the backward hemisphere with respect to the center-of-mass velocity of reactant Ar^+, suggesting that these product ions are formed via a near collinear approach, $Ar^+\cdots C-O$, $Ar^+\cdots N-N$, and $Ar^+\cdots O-O$, respectively. In the case of the $Ar^+(^2P_{3/2,1/2})$ + CO reaction, the lack of ArO^+ formed and the overwhelming intensity observed for C^+ compared to that for O^+ suggest that the attack of Ar^+ favors the C end of CO.

Both charge transfer and photoionization have long been used as experimental methods for studies of the unimolecular dissociation dynamics of state- or energy-selected ions.[52,59] Thus, it is interesting to compare the mechanisms involved in DCT and dissociative photoionization (DP). Figure 2a and 2b compares the σ values for N^+ from N_2 and O^+ from O_2 by DP and by DCT of $Ar^+(^2P_{3/2})$ + N_2 and $Ar^+(^2P_{3/2})$ + O_2 at $E_{c.m.}$ =3−131 eV, respectively.[16] Figure 3a and 3b shows the respective comparisons for the $\sigma(C^+)$ and $\sigma(O^+)$ values from DP of CO and from DCT of $Ar^+(^2P_{3/2})$ + CO.[16] Previous studies[59] have indicated that N^+ from N_2, O^+ from O_2, and C^+ and O^+ from CO by DP are produced via the predissociative excited states of N_2^+, O_2^+, and CO^+ as marked in Figures 2a, 2b, 3a, and 3b. The similar cross section profiles for N^+, C^+, and O^+ observed in DP and in DCT suggest that the N^+ (C^+,O^+) ions from DP and DCT processes involve a similar set of predissociative states of N_2^+ (CO^+,O_2^+). This charge-transfer predissociation mechanism predicts that product ions observed in DP should also be found in DCT. Due to the high cross sections for charge exchange processes, this charge-transfer predissociation mechanism also accounts for the efficient conversion of translational to electronic excitation of CO^+, N_2^+, and O_2^+, giving rise to the high σ values for N^+, C^+, O^+, ArC^+, ArN^+, and ArO^+ from $Ar^+(^2P_{3/2,1/2})$ + CO (N_2, O_2). Despite the similarity of the cross section profiles DP and DCT shown in Figures 2a, 2b, 3a, and 3c, it is interesting to note that the σ values for N^+ from N_2, O^+ from O_2, and C^+ and O^+ from CO due to DP are only about 2% of those arising from the corresponding DCT processes.

We have also obtained σ values for spin−orbit state excitation ($\sigma_{3/2\rightarrow 1/2}$) and relaxation (($\sigma_{1/2\rightarrow 3/2}$) in the $Ar^+(^2P_{3/2,1/2})$ + M (M = Ar, O_2, N_2, and CO) collisions.[6,9,10] The application of the TQDO photoionization mass spectrometer for absolute total state-to-state spin−orbit excitation and relaxation cross section measurements has been described previously.[6] The observed $\sigma_{3/2\rightarrow 1/2}$ values at low $E_{c.m.}$'s for M = O_2, N_2, and CO are found to be significantly higher than those for M = Ar. This observation is consistent with the stepwise charge-transfer mechanism of reaction 2

$$Ar^+(^2P_{3/2}) + CO\ (N_2, O_2) \rightarrow CO^+\ (N_2^{\ +}, O_2^{\ +}) + Ar \rightarrow Ar^+(^2P_{1/2}) + CO\ (N_2, O_2). \quad (2)$$

The involvement of the intermediate CO^+ (N_2^+, O_2^+) + Ar charge transfer state enhances indirectly the coupling of the reactant $Ar^+(^2P_{3/2})$ + CO (N_2, O_2) and product $Ar^+(^2P_{1/2})$ + CO (N_2, O_2) states. The theoretical prediction[61] for $\sigma_{3/2\rightarrow 1/2}$(CO) calculated at E_{lab} = 5 eV agrees with the experimental result.[9]

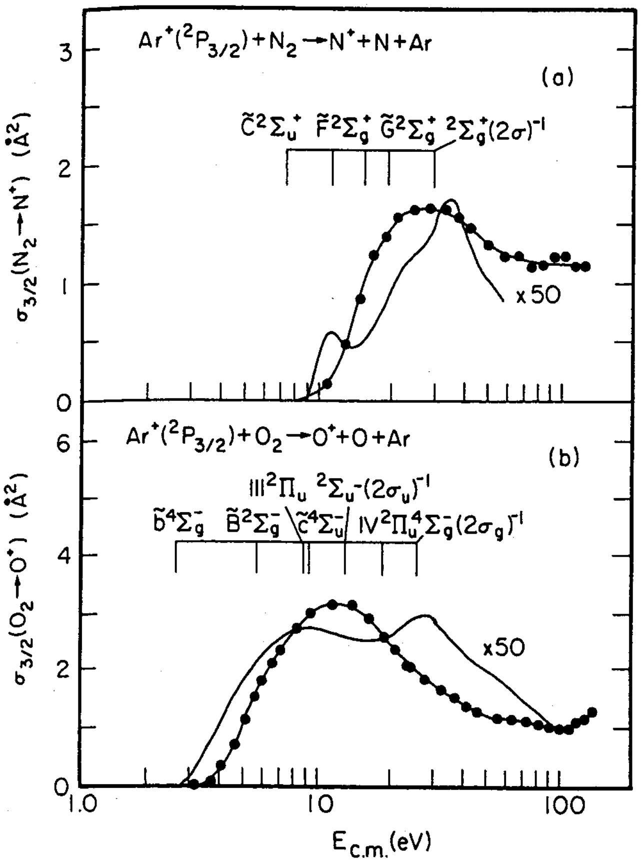

Figure 2. (a) (●) Absolute total cross sections for N^+ from $Ar^+(^2P_{3/2})$ + N_2; (—) absolute total cross sections for N^+ from photoionization of N_2. (b) (●) Absolute total cross sections for O^+ from $Ar^+(^2P_{3/2})$ + O_2; (—) absolute total cross sections for O^+ from photoionization of O_2.[6,12,13,16]

To examine further the similarities and differences between DP and DCT processes, we have also performed cross section measurement on the DCT reaction of $Ar^+(^2P_{3/2,1/2})$ + CO_2.[16] The formation CO^+ + O, O^+ + CO, and C^+ + 2O by DP of CO_2 has been well studied.[60] The previous photoionization and photoelectron studies indicate that the predissociation of excited $CO_2^+(C^2\Sigma_g^+)$ and CO_2^+(MET I−VI) states[60] is responsible for the formation of CO^+, O^+, and C^+, where MET represents multielectronic transition states. On the basis of the charge-transfer predissociation mechanism described above, we predict that product CO_2^+, CO^+, C^+, O^+, $ArCO^+$, ArC^+, and ArO^+ ions are formed in the $Ar^+(^2P_{3/2,1/2})$ + CO_2 reaction. In accord with this prediction, these product ions are observed in the reaction of $Ar^+(^2P_{3/2,1/2})$ + CO_2.

Figure 4b shows the $\sigma_{3/2}(CO_2^+)$ values from $Ar^+(^2P_{3/2})$ + CO_2 at $E_{c.m.}$ = 0.26−131 eV.[16] The $\sigma_{3/2}(CO_2^+)$ exhibits a minimum of 1.4 Å^2 at $E_{c.m.} \approx$ 10−12 eV, and increases rapidly toward lower $E_{c.m.}$. This observation of a rapid increase in cross section as $E_{c.m.}$ is decreased toward thermal energies is in qualitative accord with the Langevin−Gioumousis−Stevenson (LGS) orbiting complex model.[62] As shown in Figure 4c, the ratio $\sigma_{1/2}(CO_2^+)/\sigma_{3/2}(CO_2^+)$ is found to vary in the range of ~0.5−0.8 at $E_{c.m.}$ = 0.26−131 eV, indicating that the $\sigma_{1/2}(CO_2^+)$ is lower than $\sigma_{3/2}(CO_2^+)$. Figure 4a compares the sum of $\sigma_{3/2}$ values for CO^+, C^+, O^+, ArO^+, ArC^+, and $ArCO^+$ formed by the $Ar^+(^2P_{3/2})$ + CO_2 reaction with the sum of σ vales for CO^+, C^+, and O^+ produced from DP of CO_2. The sum of $\sigma_{3/2}$ values for CO_2^+, CO^+, C^+, O^+, ArO^+, ArC^+, and $ArCO^+$ is also plotted in Figure 4b, showing that the $\sigma_{3/2}$ values for the dissociative and reactive channels when energetically allowed

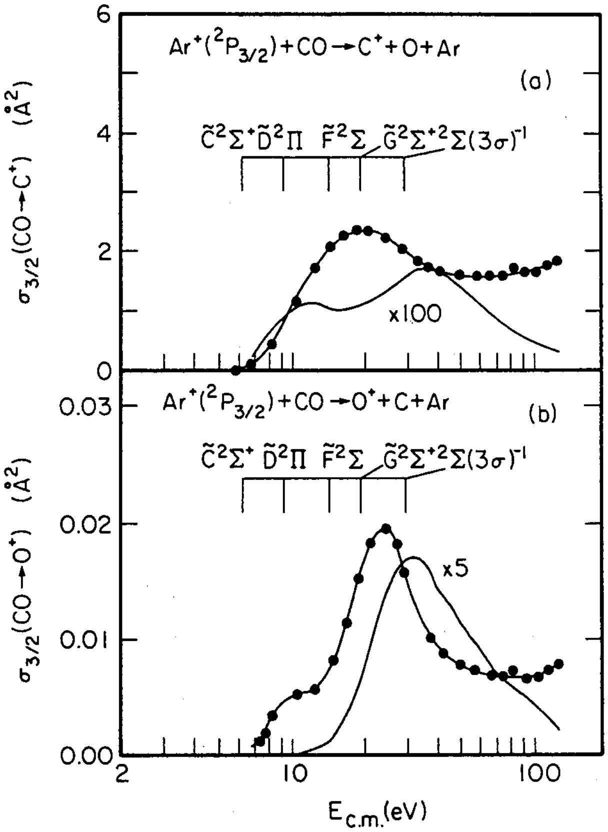

Figure 3. (a) (●) Absolute total cross sections for C^+ from $Ar^+(^2P_{3/2})$ + CO; (—) absolute total cross sections C^+ from photoionization of CO. (b) (●) Absolute total cross sections for O^+ from $Ar^+(^2P_{3/2})$ + CO; (—) absolute total cross sections for O^+ from photoionization of CO.[9,10,16]

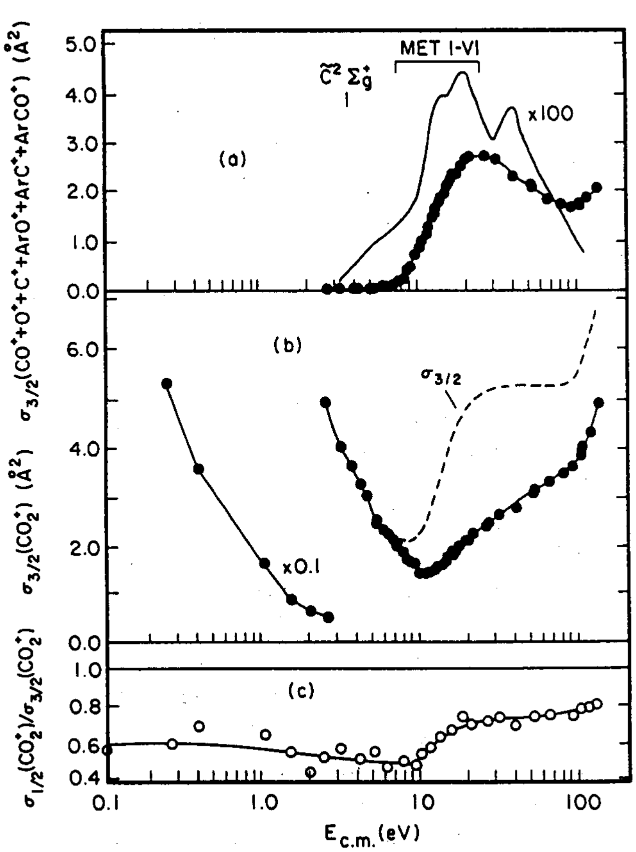

Figure 4. (a) (●) Absolute total cross sections for CO^+, O^+, C^+, ArO^+, ArC^+, and $ArCO^+$ from $Ar^+(^2P_{3/2})$ + CO_2; (—) absolute cross sections for CO^+, O^+, and C^+ from photoionization of CO_2. (b) (●) Absolute total cross sections for $CO_2{}^+$ from $Ar^+(^2P_{3/2})$ + CO_2; (- - -) the sum of absolute cross sections for $CO_2{}^+$, CO^+, O^+, C^+, $ArCO^+$, ArO^+, and ArC^+. (c) Values for the ratio $\sigma_{1/2}(CO_2{}^+)/\sigma_{3/2}(CO_2{}^+)$.[16]

are comparable to those for charge transfer. The positions of the predissociative $CO_2{}^+(C^2\Sigma_g{}^+$, MET I−VI) states are also marked in Figure 4a.

Individual $\sigma_{3/2}$ values for CO^+, O^+, and C^+ from DCT of $Ar^+(^2P_{3/2})$ + CO_2 are compared to those from DP of CO_2 in Figure 5a, 5b, and 5c.[16] The CO^+ ion is the dominant fragment compared to O^+ and C^+ formed in the $Ar^+(^2P_{3/2})$ + CO_2 reaction, whereas the cross sections for CO^+, O^+, and C^+ from DP of CO_2 are similar. The AEs observed for CO^+ ($E_{c.m.} = 4.2 \pm 0.5$ eV), O^+ ($E_{c.m.} = 3.7 \pm 0.5$ eV), and C^+ ($E_{c.m.} = 12.6 \pm 0.5$ eV) formed in the $Ar^+(^2P_{3/2})$ + CO_2 reaction are in agreement with the thermochemical thresholds for the formation of CO^+ + O, O^+ + CO, and C^+ + 2O, respectively. The maximum $\sigma_{3/2}$ values for CO^+, O^+, and C^+ formed by the DCT of $Ar^+(^2P_{3/2})$ + CO_2 are ~100-, 10-, and 35-fold, respectively, higher than corresponding σ values by DP of CO_2. Ignoring the fine structures of the cross section profiles for DP, the cross section profiles for CO^+, O^+, and C^+ formed by DCT and DP are similar. This suggests that CO^+, C^+, and O^+ ions observed in the DCT process of $Ar^+(^2P_{3/2})$ + CO_2 may also result from predissociation of excited $CO_2{}^+(C\ ^2\Sigma_g{}^+$ and MET) states. That is, similar predissociative states of $CO_2{}^+$ populated by photoionization of CO_2 are also excited efficiently by endothermic charge-transfer collisions of $Ar^+(^2P_{3/2})$ + CO_2.

The $\sigma_{3/2}$ values for $ArCO^+$, ArO^+, and ArC^+ from $Ar^+(^2P_{3/2})$ + CO_2 (Figure 6) are about 3 orders of magnitude smaller than that for $\sigma_{3/2}(CO_2{}^+)$.[16] The maximum $\sigma_{3/2}(ArC^+)$ value is about 3-fold higher than those for $\sigma_{3/2}(ArO^+)$ and $\sigma_{3/2}(ArCO^+)$. As expected, $ArO_2{}^+$ is not observed because $O_2{}^+$ is not produced in the Ar^+ + CO_2 reaction. Similar to the previous observation of ArN^+, ArO^+, and ArC^+ from $Ar^+(^2P_{3/1,1/2})$ + N_2 (O_2, CO),[9,10,12,13,16] the formation of the reactive product ions $ArCO^+$, ArO^+, and ArC^+ from $Ar^+(^2P_{3/1,1/2})$ + CO_2 are only observed in specific $E_{c.m.}$ ranges, indicating that these ions are unstable at higher $E_{c.m.}$ values.

The product kinetic energy analysis of the $Ar^+(^2P_{3/2,1/2})$ + CO_2 system is consistent with the conclusion that charge-transfer product $CO_2{}^+$ ions are mostly slow ions and scattered overwhelmingly backward with respect to the center-of-mass velocity of Ar^+. The scattering patterns for CO^+ and O^+ change from predominantly forward to backward as $E_{c.m.}$ is increased from their AEs. The ArO^+ and ArC^+ ions are backward scattered.

On the basis of the measured AEs, the $\sigma_{3/2}$ values, and the kinetic energy distributions for $CO_2{}^+$, CO^+, O^+, and C^+, we conclude that these product ions are most likely produced via a stepwise mechanism[16]

$$Ar^+(^2P_{3/2}) + CO_2 \rightarrow Ar + CO_2{}^{*+} \rightarrow Ar + O + CO^{*+} \rightarrow Ar + 2O + C^+ \text{ (or } Ar + O + C + O^+\text{)}, \quad (3)$$

where $CO_2{}^{*+}$ represents excited $CO_2{}^+$ in predissociative states. A similar mechanism has also been proposed for the formation of CO^+ and C^+ from $O^+(^4S)$ + CO_2.[15] Excited CO^{*+} produced in the dissociative charge-transfer collisions of $Ar^+(^2P_{3/2,1/2})$ + CO_2 may also dissociate to form O^+ + C. However, because the dissociation of excited CO^{*+} favors the formation of C^+, O^+ formed in process (3) may be a minor channel.[9]

The observation of the predominantly backward scattered pattern for ArO^+ and $ArCO^+$ and the forward scattered patterns for CO^+ and O^+ near their AEs is in accord with the near

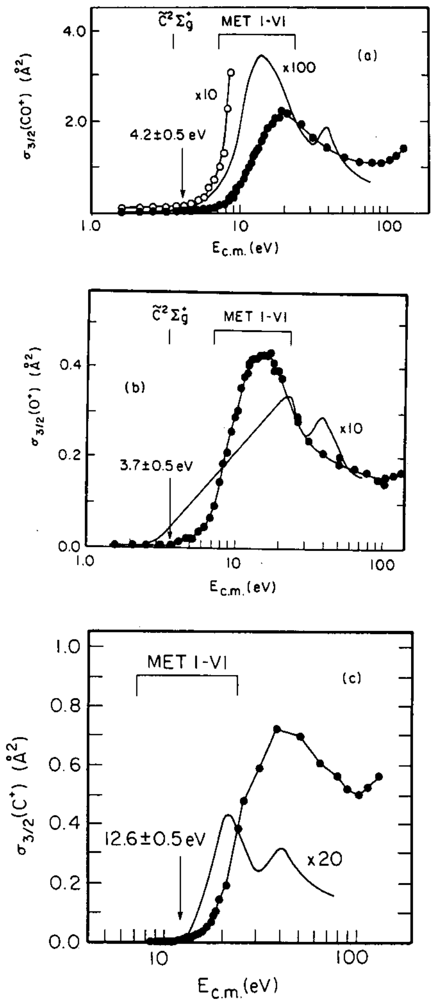

Figure 5. (a) (●) Absolute total cross sections for CO^+ from $Ar^+(^2P_{3/2})$ + CO_2; (—) absolute cross sections for CO^+ from photoionization of CO_2. (b) (●) Absolute total cross sections for O^+ from $Ar^+(^2P_{3/2})$ + CO_2; (—) absolute cross sections for O^+ from photoionization of CO_2. (c) (●) Absolute total cross sections for C^+ from $Ar^+(^2P_{3/2})$ + CO_2; (—) absolute cross sections for the formation of C^+ from photoionization of CO_2.[16]

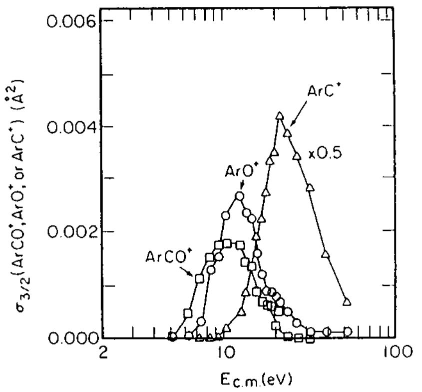

Figure 6. (□), (○), and (△) are absolute total cross sections for $ArCO^+$, ArO^+, and ArC^+ from $Ar^+(^2P_{3/2})$ + CO_2.[16]

collinear charge-transfer predissociation mechanism, which has been proposed for the formation of ArN^+ (ArO^+, ArC^+) from $Ar^+(^2P_{3/2,1/2})$ + N_2 (O_2, CO). At $E_{c.m.}$ close to the AEs of $ArCO^+$, ArO^+, CO^+, and O^+, the most effective collision geometry to convert kinetic energy into internal energies of CO_2 is the collinear $Ar^+\cdots O{-}C{-}O$ configuration, which may give rise to the formation of the collinear $Ar\cdots(O{-}C{-}O)^{*+}$ charge-transfer intermediate. The further dissociation the $(O{-}C{-}O)^{*+}$ moiety of the latter intermediate may lead to intermediates $Ar\cdots O^+\cdots CO$, $Ar\cdots O\cdots CO^+$, $Ar\cdots OC^+\cdots O$, or $Ar\cdots OC\cdots O^+$. The dissociation of $ArOC{-}O^+$ would yield $O^+ + COAr$ (or CO + Ar) with O^+ scattered mainly forward. The breaking of the $ArO^+{-}CO$ bond in a nearly collinear geometry results in the scattering of ArO^+ in the backward hemisphere. Similar dissociation processes involving $ArOC^+{-}O$ and $ArO{-}(CO)^+$ are expected to yield and $ArOC^+$ and CO^+ scattered in the backward and forward hemispheres, respectively. The theoretical study suggests that the most stable geometry for $ArCO^+$ is a linear $Ar{-}(C{-}O)^+$ structure.[61] Therefore, the formation of $Ar{-}(C{-}O)^+$ from $Ar{-}(O{-}C)^+$ may involve the rotation of the CO^+ moiety in $Ar{-}(O{-}C)^+$. The $Ar{-}(C{-}O)^+$ may also be formed from the sideway attack of Ar^+ toward the center C atom in CO_2. At $E_{c.m.}$ higher than the thresholds for the reactive ions, the charge-transfer predissociation mechanism is not limited to near collinear encounters of Ar^+ and CO_2 because the energy constraint no longer applies. The production of ArC^+ may arise from the further dissociation of excited $Ar{-}(C{-}O)^{*+}$ and/or $Ar{-}(O{-}C)^+$. These results of the $Ar^+(^2P_{3/2,1/2})$ + CO_2 experiment are in total conformity with the predictions of the predissociative charge-transfer mechanism proposed in the DCT study of $Ar^+(^2P_{3/2,1/2})$ + CO (N_2, O_2).[6]

3.2. Dissociation of CH_3SH^+, $CH_3CH_2SH^+$, and $CH_3SCH_3^+$ via Collision Activation. A bond selective process is a process that violates the expectation of a statistical outcome. Most bond selective dissociation studies have been centered on dissociation processes activated by photoexcitation. Recently, we have reported the demonstration of bond selective dissociation of CH_3SH^+, $CH_3CH_2SH^+$, and $CH_3SCH_3^+$ via collision activation.[23−26] The selective C−S and C−C bond breakages in the collision activation of these organosulfur ions are attributed to the more efficient translational to C−S and C−C vibrational transfer and inefficient energy flow between the C−S and X−H (X = C and S) vibrational modes.

In these experiments,[23−26] the organosulfur ions are prepared in their ground states by photoionization of supersonically cooled neutral parent molecules[63] at their IEs. Selected product channels for the CID reactions of CH_3SH^+ ($CH_3CH_2SH^+$, $CH_3SCH_3^+$) + Ar are given in reactions 4−13, together with their 0 K heat of reactions ($\Delta H°_0$) calculated based on known thermochemical data[64,65]

$$CH_3SH^+ + Ar \rightarrow CH_2SH^+ + H + Ar,\ \Delta H°_0 = 2.09\ \text{eV} \quad (4)$$

$$\rightarrow CH_3S^+ + H + Ar,\ \Delta H°_0 = 3.54\ \text{eV} \quad (5)$$

$$\rightarrow CH_3^+ + SH + Ar,\ \Delta H°_0 = 3.53\ \text{eV} \quad (6)$$

$$CH_3CH_2SH^+ + Ar \rightarrow CH_3CH_2^+ + SH + Ar,\ \Delta H°_0 = 1.96\ \text{eV} \quad (7)$$

$$\rightarrow CH_2SH^+ + CH_3 + Ar,\ \Delta H°_0 = 1.73\ \text{eV} \quad (8)$$

$$\rightarrow CH_3S^+ + CH_3 + Ar,\ \Delta H°_0 = 3.18\ \text{eV} \quad (9)$$

$$\rightarrow CH_3CHSH^+ + H + Ar,\ \Delta H°_0 = 1.47\ \text{eV} \quad (10)$$

$$CH_3SCH_3^+ + Ar \rightarrow CH_3SCH_2^+ + H + Ar,\ \Delta H°_0 = 2.21\ \text{eV} \quad (11)$$

$$\rightarrow CH_2SH^+ + CH_3 + Ar,\ \Delta H°_0 = 2.15\ \text{eV} \quad (12)$$

$$\rightarrow CH_3S^+ + CH_3 + Ar,\ \Delta H°_0 = 3.60\ \text{eV} \quad (13)$$

The mass 47 ions with possible structures of CH_2SH^+ and/or

CH_3S^+ are observed in all three reaction systems. It is known that CH_2SH^+ is more stable than CH_3S^+ by 1.45 eV [see processes (4), (5), (8), (9), (12), and (13)].[64,65]

To probe the structure of the mass 47 ions formed in these CID reactions, we used both the lower and upper RFOIGGCs. Reactant CH_3SH^+ ($CH_3CH_2SH^+$, $CH_3SCH_3^+$) ions formed in the photoionization region were first selected by the reactant QMS to enter the lower RFOIGGC, where the CID reaction of CH_3SH^+ ($CH_3CH_2SH^+$, $CH_3SCH_3^+$) + Ar at a given $E_{c.m.}$ took place. The mass 47 product ions thus formed were selected by the middle QMS and guided into the upper RFOIGGC, in which their structures are probed by the charge-transfer reaction with benzene (C_6H_6) at $E_{c.m.} \approx 0.2$ eV.[8] The IEs for CH_3S, CH_2SH, and C_6H_6 are known to be 9.2649 ± 0.0010 eV,[66] 7.536 ± 0.003 eV,[67] and 9.243842 ± 0.000006 eV,[68] respectively. Using these IE values, we calculate that the charge-transfer reaction 14 for CH_3S^+ is slightly exothermic by 0.0211 eV, whereas the charge-transfer reaction 15 for CH_2SH^+ is endothermic by more than 1.7 eV

$$CH_3S^+ + C_6H_6 \rightarrow CH_3S + C_6H_6^+ \quad \Delta H°_0 = -0.0211 \text{ eV} \qquad (14)$$

$$CH_2SH^+ + C_6H_6 \rightarrow CH_2SH + C_6H_6^+ \quad \Delta H°_0 = 1.708 \text{ eV} \qquad (15)$$

Charge-transfer C_6H_6+ ions formed in the upper RFOIGGC are detected by the product QMS. Because near-resonant charge transfer reactions usually have large cross sections, we should observe the formation of $C_6H_6^+$ if the mass 47 ions have the CH_3S^+ structure, whereas the charge transfer cross section should be negligibly small if CH_2SH^+ ions are produced. The probing experiments show that the mass 47 ions produced in CH_3SH^+ ($CH_3CH_2SH^+$) + Ar at $E_{c.m.} < 30$ eV have the CH_2SH^+ structure.[23−25] That is, processes (5) and (9) to form CH_3S^+ were not observed. This finding is in accord with the fact that CH_2SH^+ is significantly more stable than CH_3S^+. For the reaction of $CH_3SCH_3^+$ + Ar, the probing experiment indicates that both CH_2SH^+ and CH_3S^+ ions are produced.[8,26] Figure 7(a) shows the CID cross sections for CH_2SH^+/CH_3S^+ from $CH_3SCH_3^+$ [reactions 12 and 13], whereas the σ values for $C_6H_6^+$ resulting from the charge-transfer reaction of benzene with the mass 47 ions, which are formed in the CID reaction of $CH_3SCH_3^+$ + Ar in the $E_{c.m.}$ range of 2−6 eV, are depicted in Figure 7b.[8,26] The sharp onset observed at 3.6 ± 0.2 eV is in excellent agreement with the thermochemical threshold for reaction 13, indicating that CH_3S^+ is formed in abundance when it is energetically allowed.

Figure 8a and 8b shows the respective σ values for the CID reactions of CH_3SH^+ + Ar [reactions 4 and 6] and $CH_3CH_2SH^+$ + Ar [reactions 7 and 8].[23−25] The mass spectra observed in the CID reactions of CH_3SH^+ + Ar at $E_{c.m.}$=7.3 eV, $CH_3CH_2SH^+$ + Ar at $E_{c.m.}$=5.3 eV, and $CH_3SCH_3^+$ + Ar at $E_{c.m.}$=14 eV are shown in Figure 9a, 9b, and 9c, respectively.[22−25] These mass spectra illustrate that CH_3^+ and CH_2SH^+ from CH_3SH^+, $CH_3CH_2^+$ and CH_2SH^+ from $CH_3CH_2SH^+$, and CH_2SH^+ and CH_3S^+ from $CH_3SCH_3^+$ are the major product ions. That is, the cross sections for these product ions are significantly higher than those for other minor product ions (not shown here).

As shown in Figure 8(a), the maximum cross section of ~3.4 Å^2 for CH_3^+ is ~3 times higher than the maximum cross section of ~1.2 Å^2 for CH_2SH^+.[23,24] The AE of 3.5 ± 0.2 eV observed for CH_3^+ is in agreement with the $\Delta H°_0 = 3.53$ eV for reaction 6. This observation is consistent with the expectation that the formation of CH_3^+ + SH involves a loose transition complex and the reverse activation barrier is zero. On the basis of ab initio calculations and AE measurements by photoionization, the reverse activation for the H-elimination from the C atom of CH_3SH^+ to form CH_2SH^+ is also small ($\leq$0.07 eV).[23,24] The CID AE value of 3.9 ±0.2 eV for CH_2SH^+ from CH_3SH^+ is higher than the $\Delta H°_0$ value of 2.09 ±0.09 eV for reaction 4, indicating that the formation of CH_2SH^+ by reaction 4 is inefficient. The CID AEs for $CH_3CH_2^+$ (~1.9 eV) and CH_2SH^+ (~1.7 eV) from $CH_3CH_2SH^+$ are consistent with the $\Delta H°_0$ values of 1.96 and 1.73 eV for reactions 7 and 8, respectively.[23,25] The maximum cross section for $CH_3CH_2^+$ is ~5 Å^2 at $E_{c.m.}$ = 4−5 eV. The $\sigma(CH_2SH^+)$ from $CH_3CH_2SH^+$ at $E_{c.m.}$ = 3−30 eV are essentially constant with values of ~1.6 Å^2.

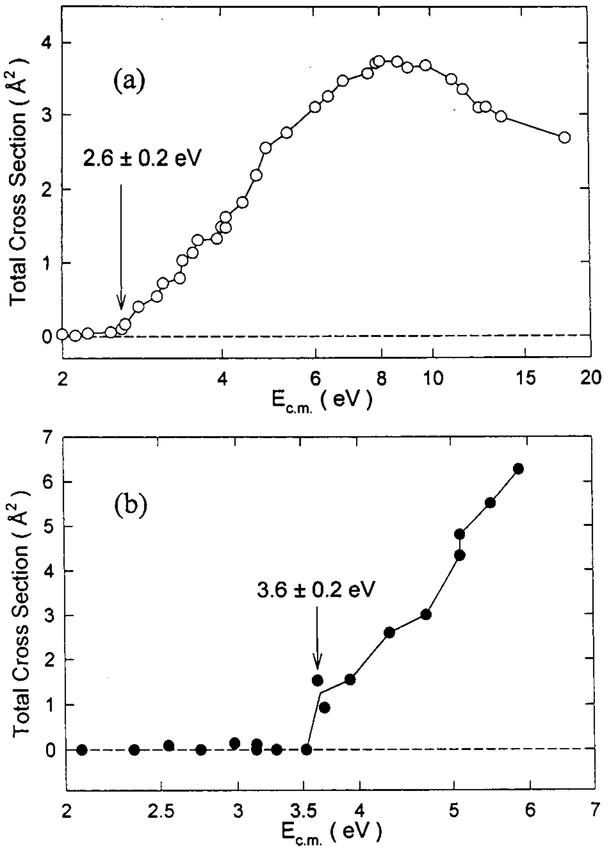

Figure 7. (a) Absolute total cross-section curve (○) for the mass 47 ion from $CH_3SCH_3^+$ + Ar at $E_{c.m.}$ = 2−20 eV; (b) Absolute cross sections (●) for C_6H_6+ observed in the charge-transfer reaction of C_6H_6 with the mass 47 ion at a fixed $E_{c.m.}$of 0.2 eV. The mass 47 ions are formed in the reaction of $CH_3SCH_3^+$ + Ar at $E_{c.m.}$ = 2−7 eV.[8,25]

The $\Delta H°_0$ values for (4)−(10) indicate that the formation of CH_2SH^+ + H is significantly more stable than the formation of CH_3^+ + SH in the CH_3SH^+ + Ar reaction, and that the formation of CH_3CHSH^+ + H channel is more stable than the $CH_3CH_2^+$ + SH and CH_2SH^+ + CH_3 channels for the reaction of $CH_3CH_2SH^+$ + Ar. On the basis of careful mass scans at various $E_{c.m.}$'s using a sufficiently high mass resolution, we conclude that CH_3CHSH^+ ions associated with the most stable product channel [reaction 10] are not produced in the CID reaction of $CH_3CH_2SH^+$ + Ar. The basic assumption of a statistical model is that the internal energy of the excited molecule is randomly distributed in the molecule's active dissociating degrees of freedom, favoring the most stable product channel. Hence, the result of this CID experiment, which shows strong preference in the formation of the higher energy product channel, is clearly incompatible with the energy randomization assumption.

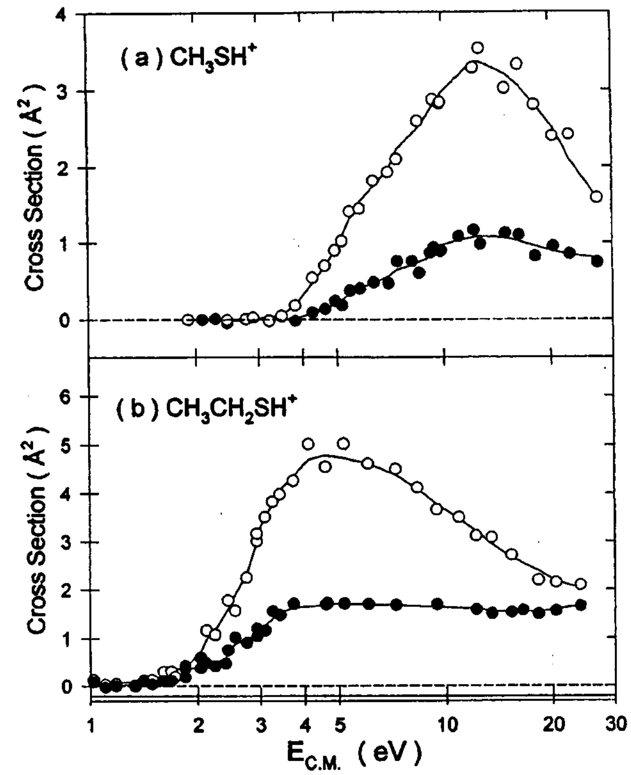

Figure 8. (a) Absolute total cross sections for CH_3^+ (○) and CH_2SH^+ (●) from CH_3SH^+ at $E_{c.m.}$=2−30 eV. (b) Absolute total cross sections for $CH_3CH_2^+$ (○) and CH_2SH^+ (●) from $CH_3CH_2SH^+$ at $E_{c.m.}$=1−30 eV.[23−25]

It is known that the collision activation at the $E_{c.m.}$ range of this experiment mainly involves translational to rotational and vibrational energy transfer. We expect that the low-frequency vibrational modes of CH_3SH^+ and $CH_3CH_2SH^+$ are preferentially excited in such a process. The highest vibrational frequencies for CH_3SH^+ and $CH_3CH_2SH^+$ correspond to the C−H and S−H stretching modes are in the range of 2500−3000 cm^{-1}, whereas the C−S stretching frequencies for CH_3SH^+ and $CH_3CH_2SH^+$ are ~700 cm^{-1} and the C−C stretching frequency for $CH_3CH_2SH^+$ is ~1200 cm^{-1}.[23−25] Thus, the internal vibrational energy resulting from collisional activation is predominantly deposited in the C−S stretching modes instead of the C−H and S−H stretching modes. The fact that the sizes of S and C are significantly greater than that of H, may also contribute to the more efficient excitation of the C−S and C−C bonds in CH_3SH^+ and $CH_3CH_2SH^+$. Owing to the large frequency differences between the C−S (C−C) and C−H (S−H) stretching modes, the C−S (C−C) and C−H (S−H) stretching modes should only be weakly coupled, resulting in inefficient energy flow between the C−S (C−C) and C−H (S−H) vibrational modes of CH_3SH^+ and $CH_3CH_2SH^+$. As a consequence, product CH_3^+ and $CH_3CH_2^+$ ions resulting from the breakage of the C−S bonds are strongly favored over those due to breakages of the C−H (S−H) bonds of CH_3SH^+ and $CH_3CH_2SH^+$. A strong bond is usually associated with a high stretching vibrational frequency. The C−H stretching frequencies for CH_3SH^+ and $CH_3CH_2SH^+$ are typical of that expected for a single C−H bond. However, the dissociation energies for the $H−CH_2SH^+$ and $H−CH(CH_3)SH^+$ bonds are significantly lower than the expected energy for a single C−H bond because of the energy gained in the C═S double bond formation in CH_2SH^+ and CH_3CHSH^+. The high vibration frequency and weak bond dissociation energy combination is a key feature for the selective CID dissociation of CH_3SH^+ and $CH_3CH_2SH^+$.

The reaction of $CH_3SCH_3^+$ + Ar can be considered as a test case for the CID dissociation mechanism gained in the CID studies of CH_3SH^+ and $CH_3CH_2SH^+$. The experimental observation of CH_3S^+ associated with the higher energy product channel [reaction 13] resulting from the C−S bond scission, can be taken as strong support for the nonstatistical CID mechanism. The AE for the mass 47 ion from the CID of $CH_3SCH_3^+$ is found to be 2.6 ± 0.2 eV.[8,26] Because this value is lower than the threshold of $\Delta H°_0$ = 3.60 eV for reaction 13, we conclude that CH_2SH^+ is also formed near its threshold. The lower energy channel corresponding to the formation $CH_3SCH_2^+$ + H from the CID reaction of $CH_3SCH_3^+$ + Ar is not found in mass scans recorded at various $E_{c.m.}$'s using a sufficiently high mass resolution.[26]

We note that the relative abundances of product ions from the dissociation of CH_3SH^+, $CH_3CH_2SH^+$, and $CH_3SCH_3^+$ observed in previous photoionization and charge exchange studies are in qualitative agreement with predictions of the statistical quasi-equilibrium theory, indicating that the energy randomization assumption is mostly valid when the internal energies of CH_3SH^+, $CH_3CH_2SH^+$, and $CH_3SCH_3^+$ are deposited by electronic excitation.[8,23−26] It is known that electronic excitation by collision activation is highly inefficient.

3.3. State-Selected Reactions Involving $O^+(^4S, ^2D, ^2P)$.

We have developed an experimental scheme for the state-selection of $O^+(^2P)$ or $O^+(^2D)$ or $O^+(^4S)$ using the TQDO mass spectrometer.[18] This scheme combines the use of the dissociative charge-transfer reactions 16−18 and the RF octopole ion trap technique

$$He^+ + O_2 \rightarrow O^+(^4S, ^2D, ^2P) + O(^3P, ^1D, ^1S) + He \quad (16)$$

$$Ne^+ + O_2 \rightarrow O^+(^4S, ^2D) + O(^3P) + Ne \quad (17)$$

$$Ar^+(^2P_{3/2,1/2}) + O_2 \rightarrow O^+(^4S) + O(^3P) + Ar \quad (18)$$

The branching ratios for the formation of $O^+(^4S)$, $O^+(^2D)$, and $O^+(^2P)$ by reaction 16 have been measured as a function of $E_{c.m.}$ in great detail in previous crossed-beam and RF octopole ion guide experiments.[3,17] The formations of $O^+(^2D)$ and $O^+(^4S)$ by reactions 17 and 18, respectively, are endothermic. We have demonstrated that $O^+(^2D)$ and $O^+(^4S)$ are produced efficiently by these reactions at $E_{c.m.}$'s above their respective thresholds. In this experiment,[18] He^+ (Ne^+, Ar^+) ions formed in the electron impact ion source are extracted and mass-selected by the reactant QMS before reacting with O_2 in the lower RFOIGGC. State-selected $O^+(^4S, ^2D, ^2P)$ reactant ions prepared by processes (16)−(18) in the lower RFOIGGC (using the procedures described below) are mass-selected by the middle QMS and further guided into the upper RFOIGGC to react with neutral reactants of interest. The intensities of reactant O^+ and product ions formed in the upper RFOIGGC are measured using the product QMS and the ion detector. Thus, absolute total cross section measurements of ion−molecule reactions involving $O^+(^4S, ^2D, ^2P)$ in this experiment have fully utilized the QMS−RFOIGGC-QMS−RFOIGGC-QMS arrangement.

The principle applied here to form an O^+ ion beam in the nearly pure $O^+(^2P)$ [or $O^+(^2D)$] state is based on the fact that $O^+(^2P)$ [$O^+(^2D)$] ions formed by reaction 16 [reaction 17] in the lower RFOIGGC possess lower kinetic energies than those for $O^+(^2D, ^4S)$ [$O^+(^4S)$] ions. By choosing appropriate V_o and ω values applied to the lower RF octopole ion guide, $O^+(^2D, ^4S)$ [$O^+(^4S)$] ions formed with higher kinetic energies can be released, whereas the majority of $O^+(^2P)$ [$O^+(^2D)$] ions with lower kinetic energies are collected and guided toward the middle QMS.[18] We note that a finite fraction of unwanted O^+(^{2}D, ^{4}S) [O^+(^{4}S)] ions originally scattered along the lower RF octopole ion guide come through the ion guide together with trapped O^+(^{2}P) [O^+(^{2}D)] ions. Assuming that the O^+ ions are scattered isotropically, the fraction of unwanted O^+(^{2}D, ^{4}S) [O^+(^{4}S)] is determined by the solid angle sustained by the exit of the octopole. For the lower RF octopole (r_o = 0.5 cm, length of rods = 18 cm) used in this experiment, the O^+(^{2}D, ^{4}S) or [O^+(^{4}S)] ions transmitted the lower octopole are ≤0.16%.[18]

We have performed characterization of O^+(^{2}D) and O^+(^{2}P) prepared using the experimental scheme described above. In the ion−molecule reaction of $O^+(^4S) + CO_2$, we find that the AE for CO^+ is in accord with its thermochemical threshold of 5.93 eV for reaction 19[18]

$$O^+(^4S) + CO_2 \rightarrow CO^+ + O + O \tag{19}$$

For reactions 20 and 21 involving reactant O^+(^{2}D) and O^+(^{2}P), the experimental onsets should shift lower to the respective thresholds of 2.63 and 0.91 eV

$$O^+(^2D) + CO_2 \rightarrow CO^+ + O + O \tag{20}$$

$$O^+(^2P) + CO_2 \rightarrow CO^+ + O + O \tag{21}$$

The σ values for reactions 19−21 at E_{cm} =1−30 eV characteristic of O^+(^{4}S), O^+(^{2}D), and O^+(^{2}P) prepared by the above scheme are depicted in Figure 10. These σ values rise from their onsets and reach a constant value of 0.4 Å^2 for O^+(^{4}S), 2 Å^2 for O^+(^{2}D), and 4.7 Å^2 for O^+(^{2}P). The σ(CO^+) values for O^+(^{4}S) of Figure 10 agree with those obtained using O^+(^{4}S) reactant ions formed by the DP of O_2. As expected, the experimental AEs for reactions 20 and 21 are in good agreement with their corresponding thermochemical thresholds, indicating that the O^+ ion beams prepared in this experiment consist of predominantly O^+(^{2}P) and O^+(^{2}D), respectively.

The accuracy of cross-section measurements at low $E_{c.m.}$'s depends in part on the laboratory kinetic energy spread (ΔE_{ab}) of the reactant ion beam. For O^+ reactant ions prepared by reactions 16−17 in the lower RFOIGGC, the ΔE_{lab} value of O^+ ions is determined mainly by the exothermicity of the ion−molecule processes involved. It is also known that in passing through a QMS, the radial kinetic energies of reactant ions may be altered, resulting in a broader ion kinetic energy distribution. The ΔE_{lab} value is found to depend on the RF amplitude supplied to the QMS. To overcome these difficulties, we have developed a simple differential retarding potential method, which can be used to reduce the ΔE_{lab} of reactant ions prepared by an ion−molecule reaction in the ion source.[69] The principle of this method is similar to the retarding potential difference method introduced previously by Fox et al.[70] to obtain a higher energy resolution of an electron beam. In essence, the differential retarding potential method achieves a narrower kinetic energy distribution by taking the difference between a nonretarded and a retarded kinetic energy distribution of the reactant ions. To implement the differential retarding potential method in the application of the TQDO apparatus, two electrostatic lenses situated between the middle QMS (10) and the upper RF octopole ion guide (11) are used as the retarding lenses. We have shown that a reactant ion beam with ΔE_{lab} of 2 eV can be reduced to 0.5 eV using this method. By employing the differential retarding potential method, together with the experimental scheme for state-selection of O^+(^{4}S, ^{2}D, ^{2}P) described above, we have obtained σ values for the O^+(^{4}S, ^{2}D, ^{2}P) + N_2 (O_2, H_2, D_2, H_2O) reactions. Selected results are briefly discussed below.[12,14−22]

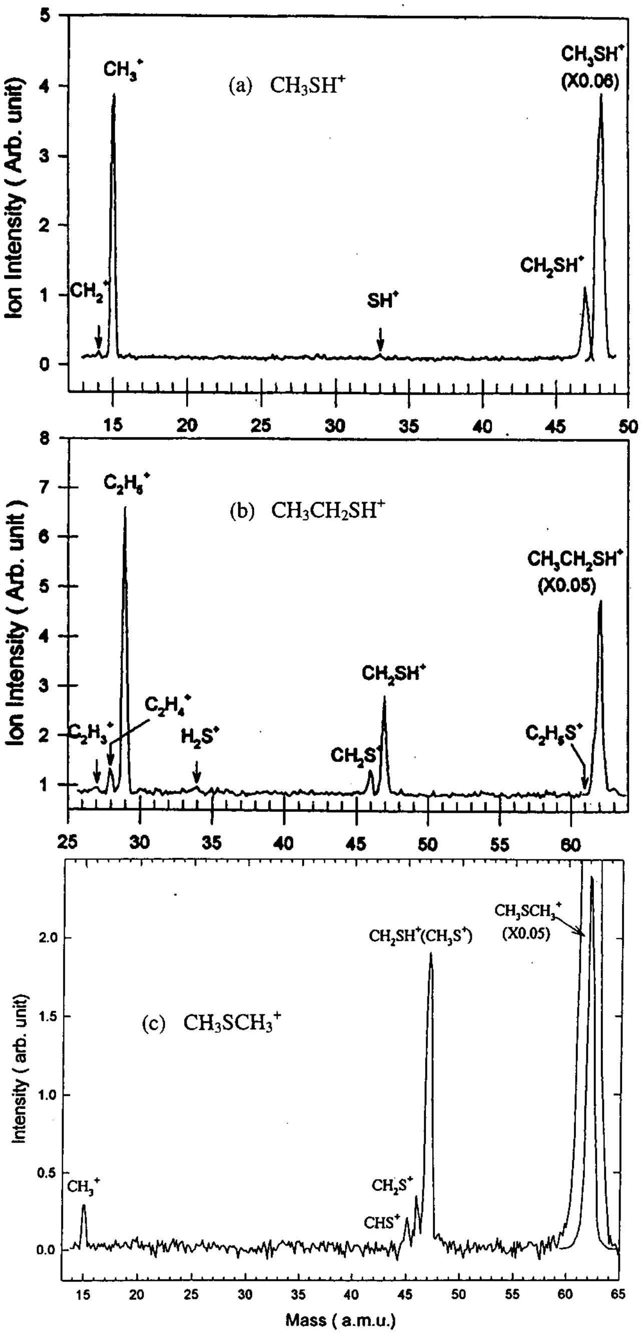

Figure 9. (a) Mass spectrum in the mass range of m/e =12−49 amu for the CID reaction of CH_3SH^+ + Ar at $E_{c.m.}$=7.3 eV.[23,24] (b) Mass spectrum in the mass range of m/e = 36−64 amu for the CID reaction of $CH_3CH_2SH^+$ at $E_{c.m.}$=5.3 eV.[23,25] (c) Mass spectrum in the mass range of m/e = 13−66 amu for the CID reaction of $CH_3SCH_3^+$ + Ar at $E_{c.m.}$ = 14 eV.[26] On the basis of careful mass scans at various $E_{c.m.}$'s using sufficiently high mass resolutions, we conclude that CH_3CHSH^+ and $CH_3SCH_2^+$ are not produced in the CID reactions of $CH_3CH_2SH^+$ + Ar and $CH_3SCH_3^+$ + Ar, respectively, within the uncertainties of $\pm 5 \times 10^{-18}$ cm^2 for these experiments.[23−26]

For $O^+(^4S) + H_2$, the formation of OH^+ is known to dominate at low $E_{c.m.}$'s. Figure 11(a) compares the σ(OH^+) values formed by the reactions O^+(^{4}S, ^{2}D, ^{2}P) + H_2 at $E_{c.m.}$ = 0.02−10 eV.[13,21] The trend and magnitude for σ(OH^+) at low $E_{c.m}$'s. roughly follow the prediction by the LGS model (see dashed line in Figure 11a).[62] The drop of σ(OH^+) at higher $E_{c.m.}$'s arises from the further dissociation of excited product OH^+. The lower σ-

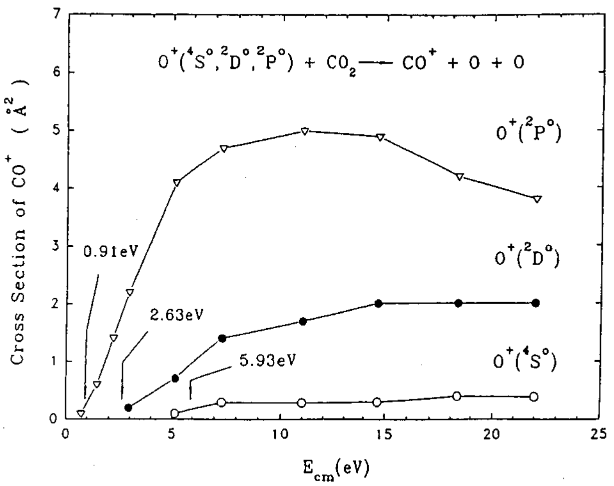

Figure 10. Absolute total cross sections for reactions 19−21 at $E_{cm} \approx 1-30$ eV characteristics of $O^+(^4S°)$ (●), $O^+(^2D°)$ (○), and $O^+(^2P°)$ (▽) prepared by reactions 16−18.[18]

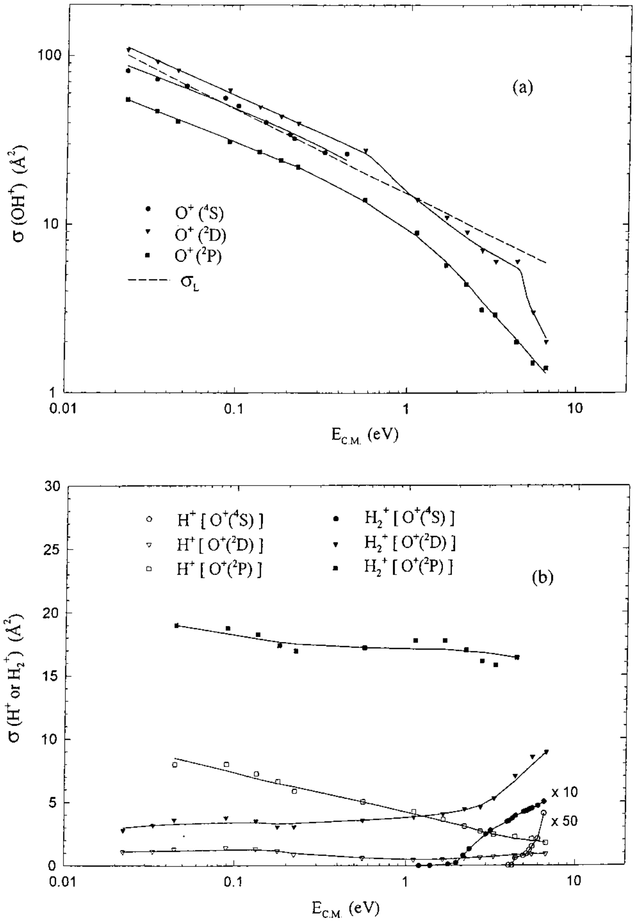

Figure 11. (a) Absolute total cross sections for OH^+ from $O^+(^4S) + H_2$, $O^+(^2D) + H_2$, and $O^+(^2P) + H_2$ at $E_{c.m.} = 0.02-7$ eV. The LGS cross sections are given by the dashed line. (b) Cross sections for H^+ and $H_2{}^+$ from the reactions of $O^+(^4S, ^2D, ^2P) + H_2$ at $E_{c.m.} = 0.02-7$ eV.[22]

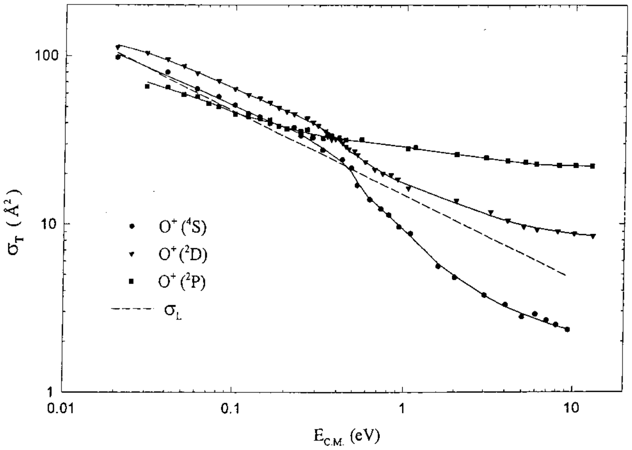

Figure 12. Comparison of σ_T values for the reactions $O^+(^4S) + H_2$, $O^+(^2D) + H_2$, and $O^+(^2P) + H_2$ at $E_{c.m.} = 0.02-7$ eV.[22]

(OH^+) from $O^+(^2P) + H_2$ can be account for by the significantly higher $\sigma(H_2{}^+)$ and $\sigma(H^+)$ from $O^+(^2P) + H_2$ as shown in Figure 11b. As expected, the $\sigma(H_2{}^+)$ and $\sigma(H^+)$ from $O^+(^4S) + H_2$ are significantly lower than those from $O^+(^2D, ^2P) + H_2$. The AEs for $H_2{}^+$ (1.70 ± 0.10 eV) and H^+ (4.60 ± 0.10 eV) from $O^+(^4S)$ are in excellent agreement with their thermochemical thresholds. The formations of $H_2{}^+$ and H^+ from $O^+(^2D, ^2P) + H_2$ are exothermic. In the $E_{c.m.}$ range of 0.04−5.0 eV, the $\sigma(H_2{}^+)$ and $\sigma(H^+)$ from $O^+(^2P) + H_2$ are in the range of 16−19 Å^2 and 2−8 Å^2, respectively. Figure 12 depicts the sum (σ_T) of the σ values for OH^+, $H_2{}^+$, and H^+ at $E_{c.m.} = 0.02-7$ eV for the individual reactions $O^+(^4S, ^2D, ^2P) + H_2$. It is interesting to note that the σ_T values for the three $O^+(^4S, ^2D, ^2P)$ states at $E_{c.m.} < 4$ eV agree within 25%. The higher σ_T values for $O^+(^2D, ^2P) + H_2$ at $E_{c.m.} > 4$ eV compared to those for $O^+(^4S) + H_2$ can be attributed to the larger numbers of opened channels for $O^+(^2D, ^2P) + H_2$. The discussion above on $O^+(^4S, ^2D, ^2P) + H_2$ also applied to $O^+(^4S, ^2D, ^2P) + D_2$ (results not shown here).

Figure 13(a) compares the $\sigma(H_2O^+)$ from $O^+(^4S) + H_2O$, $O^+(^2D) + H_2O$, and $O^+(^2P) + H_2O$ in the $E_{c.m.}$ range of 0.15−50 eV.[17,20] The charge-transfer cross sections for these reactions are found to be ~100 Å^2 at $E_{c.m.} = 0.15$ eV and to decrease rapidly as $E_{c.m.}$ is increased. This observation is consistent with the conclusion that the reactions of $O^+(^4S, ^2D, ^2P) + H_2O$ take place via a long-lived complex mechanism at low $E_{c.m.}$'s. At $E_{c.m.} < 0.5$ eV, the $\sigma(H_2O^+)$ values from $O^+(^2D) + H_2O$ are ~10% higher than those from $O^+(^4S) + H_2O$. This difference increases to ~60−100% in the $E_{c.m.}$ range of 1−30 eV. The higher $\sigma(H_2O^+)$ for $O^+(^2D) + H_2O$ compared to those for $O^+(^4S) + H_2O$ can also be rationalized by the fact that the number of available product channels for $O^+(^2D) + H_2O$ is greater than that for $O^+(^4S) + H_2O$. Although the $\sigma(H_2O^+)$ from $O^+(^2P) + H_2O$ are comparable to those from $O^+(^4S) + H_2O$ at $E_{c.m.} \geq 1$ eV, the $\sigma(H_2O^+)$ from $O^+(^2P) + H_2O$ are significantly lower than those from $O^+(^4S, ^2D) + H_2O$ at $E_{c.m.} < 1$ eV. The $\sigma(OH^+)$ from $O^+(^4S) + H_2O$, $O^+(^2D) + H_2O$, and $O^+(^2P) + H_2O$ are compared in Figure 13b,[17,20] showing that the $\sigma(OH^+)$ from both $O^+(^2D) + H_2O$ and $O^+(^2P) + H_2O$ are significantly higher than those from $O^+(^4S) + H_2O$. The $E_{c.m.}$ dependencies of the $\sigma(OH^+)$ curves for the three O^+ reactant states are different. The $\sigma(OH^+)$ curve associated with $O^+(^2D)$ gradually rises from $E_{c.m.} = 0.1$ eV and shows a broad peak at ~0.8 eV, only to decrease slowly toward higher $E_{c.m.}$'s. Stemming from the fact that significant intensities of OH^+ are observed at $E_{c.m.}$ below the thermochemical threshold for $OH^+ + O + H$, we conclude that the exothermic channel $OH^+ + OH$ also plays an important role in the production of OH^+. The decrease of $\sigma(OH^+)$ at higher $E_{c.m.}$ (>1.74 eV) may be accounted for in part by the further dissociation of internally excited OH^+ into $O^+ + H$. The $\sigma(OH^+)$ values from $O^+(^2P) + H_2O$ are relatively high, reaching values >30 Å^2 in the thermal energy range. We note that both the productions of $OH^+ + OH$ and $OH^+ + O + H$ from O^+-

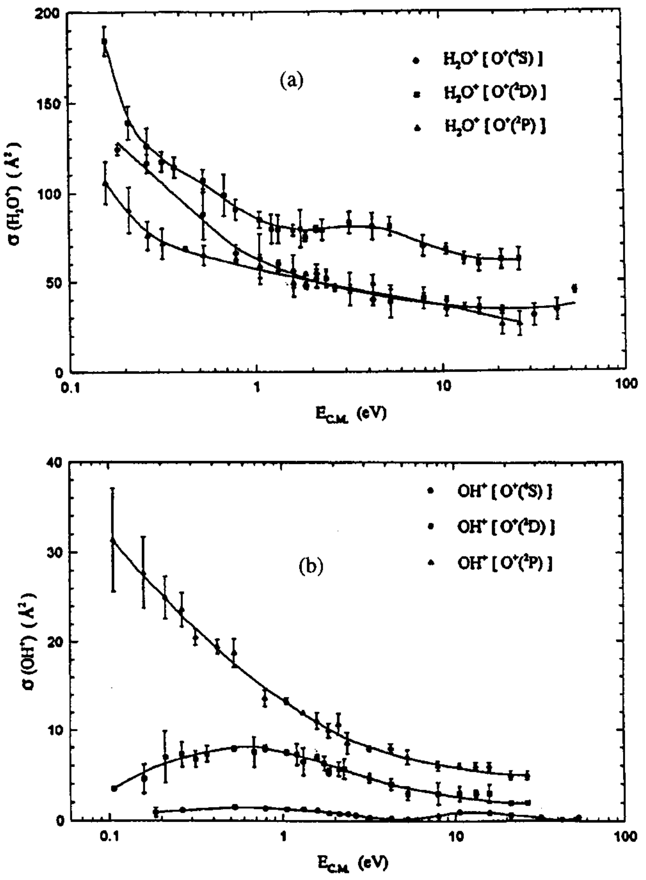

Figure 13. (a) Comparison of the $\sigma(H_2O^+)$ from $O^+(^4S) + H_2O$, $O^+(^2D) + H_2O$, and $O^+(^2P) + H_2O$ at $E_{c.m.} = 0.15-50$ eV. (b) Comparison of the $\sigma(OH^+)$ from $O^+(^4S) + H_2O$, $O^+(^2D) + H_2O$, and $O^+(^2P) + H_2O$ at $E_{c.m.} = 0.10-50$ eV.[20]

$(^2P) + H_2O$ are exothermic. The $E_{c.m.}$ dependencies for $\sigma(OH^+)$ and $\sigma(H_2O^+)$ from $O^+(^2P) + H_2O$ are similar and are characteristic of an exothermic process occurring via a long-lived complex mechanism. The competition of the $OH^+ + OH$ product channel may also account for the low $\sigma(H_2O^+)$ from $O^+(^2P) + H_2O$.

Because H_2O has a large dipole moment (μ), the leading two terms of the long-range potential for the O^+-H_2O system is $V(r) = -\alpha q^2/(2r^4) - (\mu q/r^2)\cos\theta$, where α is the isotropic dipole polarizability of H_2O, q is the charge of O^+, and θ is the angle between the dipole axis and the line connecting the centers of gravity of the two colliding partners.[62] The first term is the ion-induced dipole potential and the second term is the ion−dipole potential. The capture cross sections corresponding to the ion-induced dipole and ion−dipole potentials are $\pi q(2\alpha/E_{c.m.})^{1/2}$ and $\pi q(\mu/E_{c.m.})\cos\theta$, respectively. For large impact parameter interactions, the ion−dipole potential dominates and the capture cross section is proportional to $1/E_{c.m.}$. This condition is expected at sufficiently low $E_{c.m.}$'s, where the ion−dipole interaction plays a dominant role in the formation of long-lived collision complexes and the dipole is oriented to maximize the ion−dipole interaction during the collision. Figure 14 compares the plots of σ_T versus $1/E_{c.m.}$ for $O^+(^4S) + H_2O$, $O^+(^2D) + H_2O$, and $O^+(^2P) + H_2O$ at $E_{c.m.} = 0.15-10$ eV. The solid lines are the linear least-squares fits to the data sets. These data sets conform reasonably well with the linear fits after taking into account the experimental uncertainties. However, we note that the fit to the cross section data at $E_{c.m.} > 1$ eV is likely fortuitous because the collision times at these $E_{c.m.}$'s are too short for the molecules to reorient during the collisions.

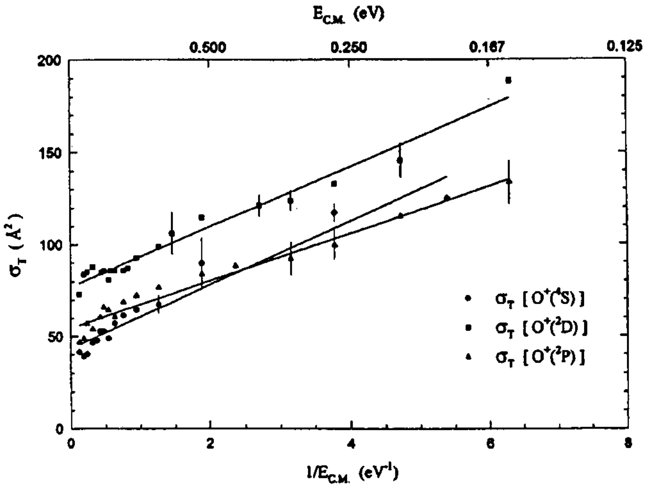

Figure 14. Plots of σ_T versus $1/E_{c.m.}$ at $E_{c.m.} = 0.15-10$ eV for $O^+(^4S) + H_2O$, $O^+(^2D) + H_2O$, and $O^+(^2P) + H_2O$.[20]

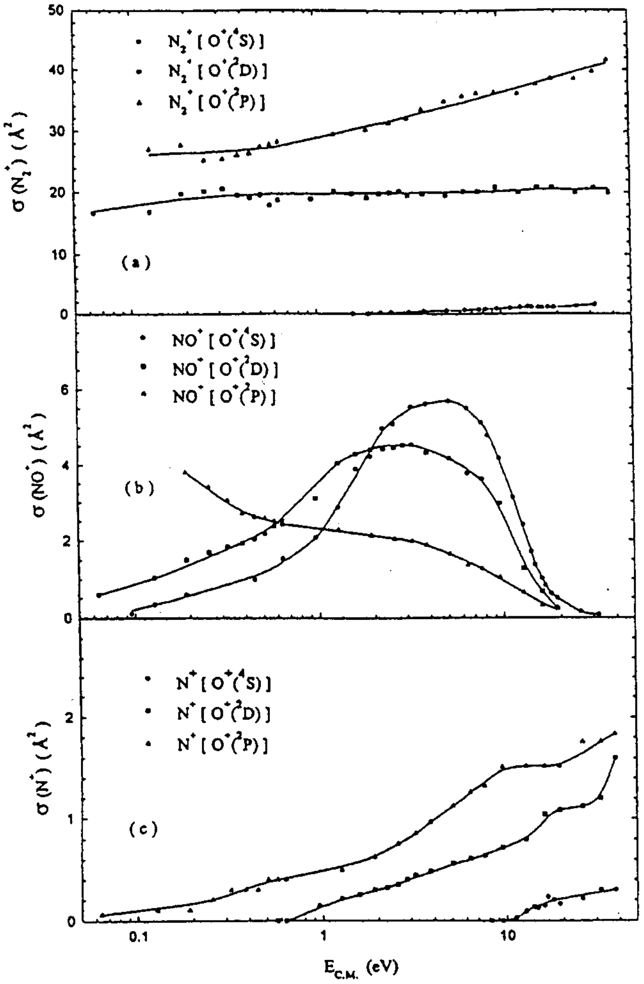

Figure 15. Comparison of (a) N_2^+, (b) NO^+, and (c) N^+ cross sections from reactions involving different $O^+(^4S, ^2D, ^2P)$ electronic states.[21]

The σ values for N_2^+, NO^+, and N^+ from $O^+(^4S, ^2D, ^2P) + N_2$ in the $E_{c.m.}$ range of 0.06−40 eV are compared in Figure 15a, 15b, and 15c, respectively.[11,19,21] As shown in Figure 15(a), it is obvious that the charge-transfer efficiencies of $O^+(^2P)$ and $O^+(^2D)$ to N_2 are significantly greater than that for $O^+(^4S)$ to N_2. The ratio of $\sigma(N_2^+)$ for $O^+(^2D) + N_2$ to that for $O^+(^2P) + N_2$ varies from ~0.75 at $E_{c.m.} \approx 0.1$ eV to 0.5 at $E_{c.m.} = 40$ eV. Figure 15b shows that the profiles for $\sigma(NO^+)$ from $O^+(^4S) + N_2$ and $O^+(^2D) + N_2$ are similar except that the profile

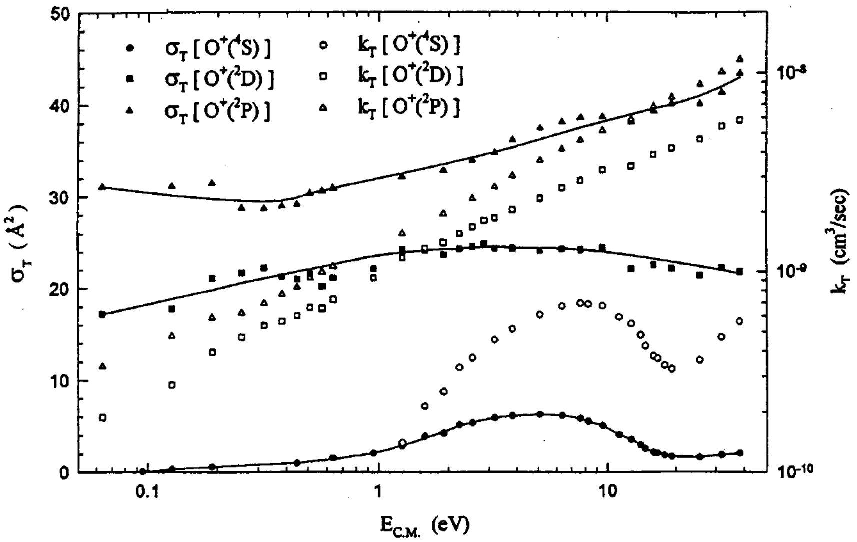

Figure 16. Comparison of σ_T values for the reactions $O^+(^4S) + N_2$, $O^+(^2D) + N_2$, and $O^+(^2P) + N_2$. Here, $\sigma_T = \sigma(N_2^+ + NO^+ + N^+)$. The total rate constants (k_T values) corresponding to σ_T values for $O^+(^4S)$, $O^+(^2D)$]; and $O^+(^2P)$ are also included.[21]

from $O^+(^2D) + N_2$ is shifted to lower $E_{c.m.}$ by ~3 eV. The profile for $\sigma(NO^+)$ from $O^+(^2P) + N_2$ is different from those from $O^+(^4S, ^2D) + N_2$, and reveals a decreasing trend as $E_{c.m.}$ is increased. The $\sigma(NO^+)$ values from $O^+(^4S,^2D, ^2P) + N_2$ become negligible at $E_{c.m.} > 25$ eV. The $\sigma(N^+)$ values for $O^+(^4S) + N_2$, $O^+(^2D) + N_2$, and $O^+(^2P) + N_2$ shown in Figure 15c all exhibit an increasing trend as $E_{c.m.}$ is increased. The profiles for the $\sigma(N^+)$ curves associated with the excited-state reactions are shifted to lower $E_{c.m.}$'s with respect to that for the ground $O^+(^4S)$ state. The $\sigma(N^+)$ curves for $O^+(^4S) + N_2$ and $O^+(^2D) + N_2$ reveal distinct thresholds for the $N^+ + N + O$ and $N^+ + NO$ thresholds, respectively. Figure 16 compares the $\sigma_T = \sigma(N_2^+ + NO^+ + N^+)$ from $O^+(^4S) + N_2$, $O^+(^2D) + N_2$, and $O^+(^2P) + N_2$. The total rate constants (k_T's) for these reactions calculated using the equation $(2E_{c.m.}/\mu_r)^{1/2}$ (where μ_r is the reduced mass) and σ_T values are also plotted in Figure 16.[21] This comparison shows that the maximum σ_T values for $O^+(^2D) + N_2$ and $O^+(^2P) + N_2$ are relatively insensitive to $E_{c.m.}$. Although the maximum σ_T value for $O^+(^4S) + N_2$ is ~30% of that for $O^+(^2D) + N_2$, the σ_T values for $O^+(^2P) + N_2$ are 50–100% greater than those for $O^+(^2D) + N_2$. The higher σ values observed for the excited-state reactions can be understood by the increased number of open product channels.

We have also obtained absolute total state-selected charge-transfer cross sections for $O^+(^4S, ^2D, ^2P) + O_2$ in the $E_{c.m.}$ range of 0.05–40 eV.[71] The $\sigma(O_2^+)$ values from $O^+(^4S) + O_2$ in the $E_{c.m.}$ range of 0.05–3 eV obtained in our experiment are in the range of 0.5–4.5 Å^2 and are consistent with previous reaction rate measurements. The charge-transfer cross sections for $O^+(^2P) + O_2$ are found to be ~3-fold greater than those for $O^+(^2D) + O_2$, which in turn are ~2–20-fold higher than those for $O^+(^4S) + O_2$.[70] Because $O^+(^4S)$, $O^+(^2D)$, and $O^+(^2P)$ are produced nearly in equal intensities by solar UV dissociation and photoionization in the ionosphere, this result indicates that O_2^+ formed in the collisions of $O^+(^2D, ^2P) + O_2$ is a main source of O_2^+ ions and must be taking into consideration of a realistic modeling of the ion chemistry cycles.

4. Future Developments

The most general method for the preparation of state- or energy-selected reactant ions has been demonstrated to be the VUV TPESICO technique.[5] Due to the mediation of near-resonant autoionizing states, the TPE bands for vibronic states of photoions with negligible Franck–Condon factors for direct photoionization can be observed. However, the previous applications[5] of the TPESICO method for state-selected ion–molecule reaction experiments have been limited by the relatively low TPE resolution (~20 meV, fwhm). Furthermore, the hot-electron tail problem associated with the transmission function of TPE detection may also degrade the purity of vibronic states prepared using the TPESICO method.

The recent development of VUV lasers[72–75] and third generation synchrotron radiation source,[49–51] together with the introduction of the PFI–PE detection scheme,[76–79] has had a profound impact to the field of VUV photoelectron spectroscopy. The PFI–PE scheme is a variant of the TPE method. The PFI–PE spectra for many diatomic and polyatomic hydride species have been recorded and analyzed in the rotationally resolved level, covering energy ranges close to the ion dissociation limits.[49–51] As an example, we show in Figure 17, the rotationally resolved PFI–PE spectrum for $H_2^+(v^+ = 0–18)$ obtained using a synchrotron based PFI–PE scheme,[49] where rotational transitions of the highest level of the ground state of H_2^+, $v^+ = 18$, were resolved. We have also developed a generally applicable synchrotron based PFI–PEPICO scheme, making it possible to select the internal state or energy of ions with a resolution of ~5 cm^{-1} (fwhm),[50–58] limited only by the PFI–PE measurement. Employing this method, we have successfully examined the state-selected unimolecular dissociation reaction of $O_2^+(b^4\Sigma_g^-, v^+ = 4, N^+)$ with rotational specificity.[52] Selected PFI–PEPICO TOF spectra obtained in the energy range of 18.7227–18.7193 eV are shown in Figure 18, revealing the unimolecular dissociation yield of rovibronic state selected O_2^+ at an energy increment of 0.5 meV.[52] Effort is being made to extend the PFI–PEPICO scheme employed for unimolecular dissociation studies to the PFI–PESICO method for bimolecular reaction studies. In such experiments, the product ions resulting from bimolecular collisions, together with the unreacted reactant ions will appear in the coincidence TOF spectra similar to those shown in Figure 18. A mass spectrometer equipped with a RF octopole ion guide reaction cell, a QMS, and PFI–PE detector has been installed at the Chemical Dynamics Beamline of the Advanced Light Source. Preliminary results on state-selected ion–molecule reaction studies using the PFI–PESICO scheme have been obtained. We believe that the PFI–PESICO technique has the potential to significantly enhance the scope of state-

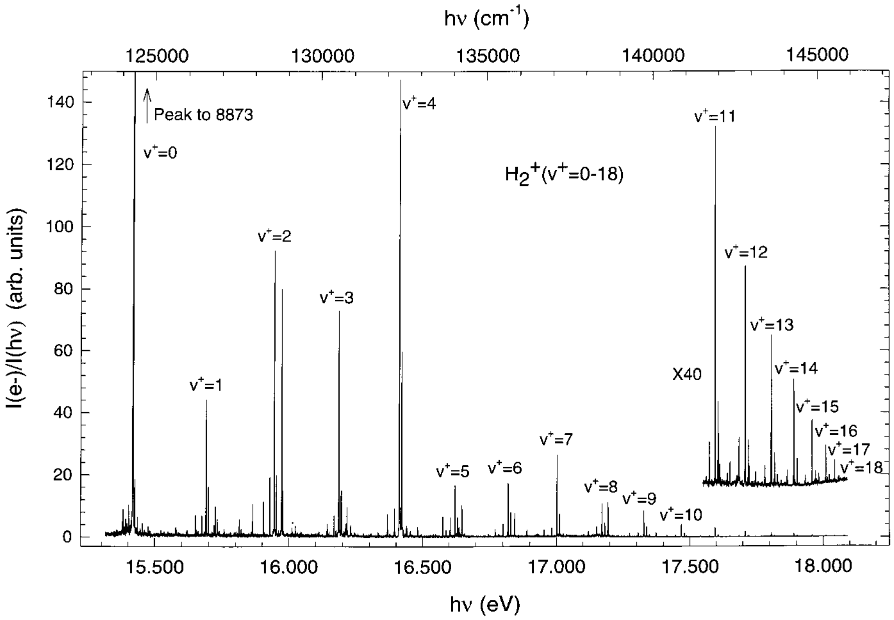

Figure 17. Rotationally resolved PFI−PE spectrum for $H_2^+(v^+ = 0-18)$ obtained using a synchrotron based PFI−PE detection scheme.[49]

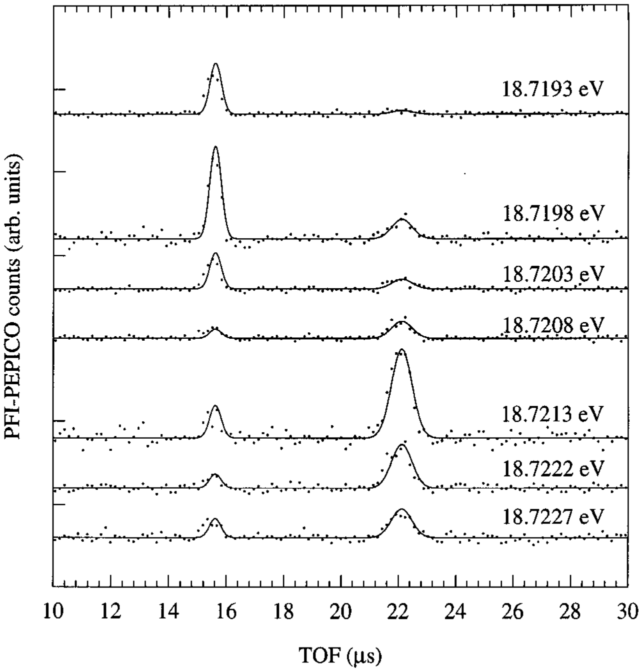

Figure 18. PFI−PEPICO TOF spectra for O^+ (peak at 15.5 μs) and O_2^+ (peak at 22.1 μs) from O_2 at 18.7193−18.7227 eV obtained using an effusive O_2 beam.[52]

selected ion−molecule reaction studies. Because both the internal state and the mass of a PFI−PI are known, the PFI−PI or MATI (mass-analyzed threshold ion) technique[80−82] is also a viable method for the preparation of rovibronic state-selected reactant ions for ion−molecule reaction studies. The PFI−PI detection scheme usually requires a relatively large dc field and a relatively long delay between the VUV excitation and PFI field to separate background prompt ions from PFI−PIs. The higher dc field used has the effect of inducing ionization of high-n Rydberg species initially populated in optical excitation and, thus, lowers the sensitivity for PFI−PI detection compared to that for PFI−PE measurements. Because of the delay requirement, pulsed lasers are more appropriate excitation light sources for the detection of PFI−PIs. The further development of the PFI−PESICO and PFI−PI methods for the preparation of state-selected reactant ions for ion−molecule reaction studies is to be anticipated.

In plasma environments, where both ions and radicals coexist, the reactions between ions and radicals are expected to be important. Currently, there is essentially no information available on rate constants or cross sections of ion−molecule reactions involving neutral radicals. The studies of state-selected ion-radical reactions should be an important and challenging future research area.

Acknowledgment. The author is indebted to former post-doctoral associates and students, X. Li, S. Nourbakhsh, Y.-J. Chen, C.-W. Hsu, M. Evans, S. Stimson, Y. Song, G. Jarvis, Y.-L. Huang, T. P. Fenn, C.-L. Liao, and G. D. Flesch, who performed the original experiments described in this article. This work was supported by the NSF Grant No. ATM-001646 and AFOSR Grant No. F49620-99-1-0234 (technical monitor: Dr. Michael Berman). Partial support by the Chemical Science Division of the U.S. Department of Energy is also acknowledged.

References and Notes

(1) Liu, K.-P.; Wagner, A. Eds. *The Molecular Dynamics and Kinetics of Radical Reactions, Part I and II*; World Scientific: Singapore, 1995. *Adv. Ser. in Phys. Chem.* Vols. **6A** and **6B**.

(2) Ng, C. Y.; Baer, M. Eds. *State-Selected and State-to-State Ion−Molecule Reaction Dynamics I: Experiment and II: Theory*; Wiley: New York, 1992. *Adv. Chem. Phys.* Vol. *82*.

(3) Gerlich, D. In. *State-Selected and State-to-State Ion−Molecule Reaction Dynamics: I. Experiment*; Ng, C. Y., Baer, M, Eds.; Wiley: New York, 1992. *Adv. Chem. Phys.* Vol. 82, p 1.

(4) Anderson, S. L. In. *State-Selected and State-to-State Ion−Molecule Reaction Dynamics: I. Experiment*; Ng, C. Y., Baer, M, Eds.; Wiley: New York, 1992. *Adv. Chem. Phys.* Vol. *82*, p 213.

(5) Koyano, I.; Tanaka, K. In *State-Selected and State-to-State Ion−Molecule Reaction Dynamics: I. Experiment*; Ng, C. Y., Baer, M, Eds.; Wiley: New York, 1992. *Adv. Chem. Phys.* Vol. 82, p 263.

(6) Ng, C. Y. In *State-Selected and State-to-State Ion−Molecule Reaction Dynamics: I. Experiment*; Ng, C. Y., Baer, M, Eds.; Wiley: New York, 1992. *Adv. Chem. Phys.* Vol. 82, p 401.

(7) Bower, M. T.; editor, *Int. J. Mass Spectrometry*, special issue for year 2000, Volume 200.

(8) Chen, Y.-J.; Fenn, P. T.; Ng, C. Y. *Chem. Phys. Lett.* **2001**, *336*, 105.

(9) Flesch, G. D.; Ng, C. Y. *J. Chem. Phys.* **1988**, *89*, 3381.

(10) Flesch, G. D.; Nourbakhsh, S.; Ng, C. Y. *J. Chem. Phys.* **1991**, *95*, 3381.

(11) Flesch, G. D.; Ng, C. Y. *J. Chem. Phys.* **1990**, *92*, 3235.

(12) Flesch, G. D.; Ng, C. Y. *J. Chem. Phys.* **1990**, *92*, 2876.

(13) Flesch, G. D.; Nourbaksh, S.; Ng, C. Y. *J. Chem. Phys.* **1990**, *92*, 3590.

(14) Flesch, G. D.; Ng, C. Y. *J. Chem. Phys.* **1991**, *94*, 2372.

(15) Flesch, G. D.; Ng, C. Y. *J. Geophys. Res.* **1991**, *96*, 21 403.

(16) Flesch, G. D.; Ng, C. Y. *J. Chem. Phys.* **1992**, *97*, 162.

(17) X.-Li.; Huang, Y.-L.; Flesch, G. D.; Ng, C. Y. *J. Chem. Phys.* **1995**, *102*, 5100.

(18) Li, X.; Huang, Y.-L.; Flesch, G. J.; Ng, C. Y. *Rev. Sci. Instrum.* **1995**, *66*, 2871.

(19) Li, X.; Stimson, S.; Flesch, G. D.; Ng, C. Y. *SPIE* **1995**, *2548*, p 305−315.

(20) Li, X.; Huang, Y.-L.; Flesch, G. D.; Ng, C. Y. *J. Chem. Phys.* **1997**, *106*, 928.

(21) Li, X.; D. Huang, Y.-L.; Flesch, G.; Ng, C. Y. *J. Chem. Phys.* **1997**, *106*, 1373.

(22) Li, X.; Huang, Y.-L.; Flesch, G. D.; Ng, C. Y. *J. Chem. Phys.* **1997**, *106*, 564.

(23) Chen, Y.-J.; Fenn, P. T.; Stimson, S.; Ng, C. Y. *J. Chem. Phys.* **1997**, *106*, 8274.

(24) Fenn, P. T.; Chen, Y. J.; Stimson, S.; Ng, C. Y. *J. Phys. Chem.* **1997**, *101A*, 6513.

(25) Chen, Y. J.; Stimson, S.; Fenn, P. T.; Ng, C. Y.; Li, W.-K.; Ma, N.-L. *J. Chem. Phys.* **1998**, *108*, 8020.

(26) Chen, Y.-J.; Lau, K.-C.; Fenn, P. T.; Ng, C. Y.; Law, C.-K.; Li, W.-K. *J. Phys. Chem*, accepted.

(27) Banks, P. M.; Kockarts, G. *"Aeronomy"*, Part A; Academic: New York, 1973, pp 14, 257.

(28) Dalgarno, A.; Fox, J. L. In *Unimolecular and Bimolecular Ion−Molecule Reaction Dynamics*; Ng, C. Y., Baer, T., Powis, I., Eds.; *Wiley Series in Ion Chem., & Phys.*; Wiley: Chichester, 1994, p 1.

(29) Park, C. *Nonequilibrium Hypersonic Aerothermodynamics*; Wiley: New York, 1990.

(30) Boyd, I. D.; Candler, G. V.; Levin, D. A. *Phys. Fluids* **1995**, *7*, 1756.

(31) Kluever, C. A. *J. Spacecraft Rockets* **1997**, *34*, 405.

(32) Bird, G. A. *Molecular Gas Dynamics and the Direct Simulation of Gas Flows*; Oxford University Press: Oxford, 1994.

(33) Boyd, I. D. *J. Propulsion and Power* **1997**, *13*, 775.

(34) Torr, D. G.; Orsini, N. *Planet. Space Sci.* **1977**, *25*, 1171.

(35) Torr, D. G.; Orsini, N. *Geophys. Res. Lett.* **1980**, *5*, 657.

(36) Torr, M. R.; Torr, D. G. *Geophys. Res. Lett.* **1980**, *7*, 103.

(37) Torr, M. R.; Torr, D. G. *Rev. Geophys. Space Phys.* **1982**, *20*, 91.

(38) Dalgarno, A.; McElroy, M. B. *Planet. Space Sci.* **1965**, *13*, 947.

(39) Henry, R. J. *Astrophys. J.* **1970**, *161*, 1153.

(40) Kohl, J. L.; Lafyatis, G. P.; Palenius, H. P.; Parkinson, W. H. *Phys. Rev.* A **1978**, *18*, 571.

(41) Ferguson, E. E.; Fehsenfeld, F. C.; Albritton, D. L. In *Gas-Phase Ion Chemistry*; Bowers, M. T., Ed.; Academic: New York, 1979; Vol. 1, p 45.

(42) Dalgarno, A. *Adv. At. Mol. Phys.* **1979**, *15*, 37.

(43) Bates, D. R.; Massey, H. S. W. *Proc. R. Soc. London Ser. A* **1947**, *192*, 1

(44) Kella, D.; Vejby-Christensen, L.; Johnson, P. J.; Pedersen, H. B.; Anderson, L. H. *Science* **1997**, *276*, 1530.

(45) Campbell, W. W. *Astrophys. J.* **1895**, *2*, 162.

(46) Mendillo, M.; Hawkins, G. S.; Klobuchar, J. A. *J. Geophys. Res.* **1975**, *80*, 2217.

(47) Watson, W. D.; *Accounts Chem. Res.* **1977**, *10*, 221.

(48) Duley, W. W.; Williams, D. A. *Interstellar Chemistry*; Academic Press: New York, 1984.

(49) Ng, C. Y. In. *Photoionization and Photodetachment*; Ng, C. Y., Ed.; World Scientific: Singapore, 2000; *Adv. Ser. Phys. Chem.*, Vol. **10A**, p. 394.

(50) Ng, C. Y. *Int. J. Mass spectrometry* **2000**, *200*, 357.

(51) Ng, C. Y.; *Annu. Rev. Phys. Chem.* **2002**, *53*, 101.

(52) Jarvis, G. K.; Weitzel, K.-M.; Malow, M.; Baer, T.; Song, Y.; Ng, C. Y. *Rev. Sci. Instrum.* **1999**, *70*, 3892.

(53) Song, Y.; Qian, X.-M.; Lau, K.-C.; Ng, C. Y.; Liu, J.; Chen, W. *J. Chem. Phys.* **2001**, *115*, 2582.

(54) Song, Y.; Qian, X.-M.; Lau, K.-C.; Ng, C. Y.; Liu, J.; Chen, W. *J. Chem. Phys.* **2001**, **115**, 4095.

(55) Qian, X.-M.; Song, Y.; Lau, K.-C.; Ng, C. Y.; Liu and W Chen, J. *Chem. Phys. Lett.* **2001**, *347*, 51.

(56) Qian, X.-M.; Song, Y.; Lau, K.-C.; Ng, C. Y.; Liu, J.; Chen, W.; He, G. Z. *Chem. Phys. Lett.* **2002**, *353*, 19.

(57) Jarvis, G. K.; Weitzel, K.-M.; Malow, M.; Baer, T.; Song, Y.; Ng, C. Y. *Phys. Chem. Chem. Phys.* **1999**, *1*, 5259.

(58) Weitzel, K.-M.; Malow, M.; Jarvis, G. K.; Baer, T.; Song, Y.; Ng, C. Y. *J. Chem. Phys.* **1999**, *111*, 8267.

(59) Lindholm, E. In. *Ion-Molecule Reactions in the Gas Phase*; Gould, R. F., Ed.; Advances in Chemistry Series, American Chemical Society: Washington, DC, 1966, *58*, 1.

(60) Gallagher, J. W.; Brian, C. E.; J. a. Samson, R.; Langhoff, P. W. *J. Phys. Chem. Ref. Data* **1988**, *17*, 1, and references therein.

(61) Gislason, E. A.; Parlant, G.; Archirel, P.; Sizun, M. *Faraday Discuss. Chem. Soc.* **1987**, *84*, 325.

(62) Gioumousis, G.; Stevenson, D. P. *J. Chem. Phys.* **1958**, *29*, 294.

(63) Morioka, Y. In. *Photoionization and Photodetachment*; Ng, C. Y., Ed.; Adv. Ser. Phys. Chem. 10A; World Scientific: Singapore, 2000; p 347.

(64) Ng, C. Y. In. *Advances in Photochemistry*; Volman, Hammond, and Neckers, Eds.; Wiley: New York, 1997; Vol. 22, Chapter 1, p 1.

(65) Ng, C. Y. In. *Energetics and Structure of Organic Ions*; Baer, T., Ng, C. Y., Powis, I., Eds.; Wiley Series in Ion Chem. & Phys.; Wiley: Chichester, 1996; p 35.

(66) Hsu, C. W.; Ng, C. Y. *J. Chem. Phys.* **1994**, *101*, 5596.

(67) Ruscic, B.; Berkowitz, J. *J. Chem. Phys.* **1992**, *97*, 1818.

(68) Neuhauser, R. G.; Siglow, K.; Neusser, H. J. *J. Chem. Phys.* **1997**, *106*, 896.

(69) Li, X.; Huang, Y.-L.; Flesch, G. D.; Ng, C. Y. *Rev. Sci. Instrum.* **1994**, *65*, 3724

(70) Fox, R. E.; Hickam, W. H.; Grove, D. J.; Kjeldaas, T., Jr. *Rev. Sci. Instrum.* **1955**, *26*, 1101.

(71) Li, X.; Huang, Y.-L.; Flesch, G. D.; Ng, C. Y., to be published.

(72) Kung, A. H.; Lee, Y. T. In. *Vacuum Ultraviolet Photoionization and Photodissociation of Molecules and Clusters*; Ng, C. Y., Ed.; World Scientific: Singapore, 1991; p 487.

(73) Hepburn, J. W. In. *Vacuum Ultraviolet Photoionization and Photodissociation of Molecules and Clusters*; Ng, C. Y., Ed.; World Scientific: Singapore, 1991; p 435.

(74) Hepburn, J. W. In. *Laser Techniques in Chemistry*; Meyers, A., Rizzo, T. R., Eds.; Wiley: New York, 1994.

(75) Hollenstein, U. Palm, H.; Merkt, F. *Rev. Sci. Instrum.* **2000**, *71*, 4023.

(76) Powis, I.; Baer, T.; Ng, C. Y. Eds. *High-Resolution Laser Photoioniztion and Photoelectron Studies*; Wiley Series in Ion Chem. & Phys.; Wiley: Chichester, 1995.

(77) Schlag, E. W. *ZEKE Spectroscopy*; Cambridge University Press: Cambridge, 1996.

(78) Müller-Dethlefs, K.; Sander, M.; Schlag, E. W. *Chem. Phys. Lett.* **1984**, *112*, 291.

(79) Reiser, G.; Habenicht, W.; Müller-Dethlefs, K.; Schlag, E. W. *Chem. Phys. Lett.* **1988**, *119*, 152.

(80) Zhu, L.; Johnson, P. *J. Chem. Phys.* **1991**, *94*, 5769.

(81) Johnson, P. M. In. *Photoionization and Photodetachment*; Ng, C. Y., Ed.; Adv. Ser Phys. Chem. 10A; World Scientific: Singapore, 2000, p 296.

(82) Jarvis, G. K.; Shiell, R. C.; Hepburn, J.; Song, Y.; Ng, C. Y. *Rev. Sci. Instrum.* **2000**, *71*, 1325.